Published in final edited form as:
Prog Neurobiol. 2022 June ; 213: 102263. doi:10.1016/j.pneurobio.2022.102263.

Cortical connectivity is embedded in resting state at columnar resolution

Nicholas S. Card[b,c,d], **Omar A. Gharbawie**[a,b,c,d,*]

[a]Department of Neurobiology, University of Pittsburgh, USA

[b]Systems Neuroscience Center, University of Pittsburgh, USA

[c]Department of Biomedical Engineering, University of Pittsburgh, USA

[d]Center for the Neural Basis of Cognition, USA

Abstract

Resting state (RS) fMRI is now widely used for gaining insight into the organization of brain networks. Functional connectivity (FC) inferred from RS-fMRI is typically at macroscale, which is too coarse for much of the detail in cortical architecture. Here, we examined whether imaging RS at higher contrast and resolution could reveal cortical connectivity with columnar granularity. In longitudinal experiments (~1.5 years) in squirrel monkeys, we partitioned sensorimotor cortex using dense microelectrode mapping and then recorded RS with intrinsic signal optical imaging (RS-ISOI, 20 μm/pixel). FC maps were benchmarked against microstimulation-evoked activation and traced anatomical connections. These direct comparisons showed high correspondence in connectivity patterns across methods. The fidelity of FC maps to cortical connections indicates that granular details of network organization are embedded in RS. Thus, for recording RS, the field-of-view and effective resolution achieved with ISOI fills a wide gap between fMRI and invasive approaches (2-photon imaging, electrophysiology). RS-ISOI opens exciting opportunities for high resolution mapping of cortical networks in living animals.

Keywords

Resting state; Cortical connectivity; Intrinsic signal optical imaging; FMRI; Sensorimotor cortex; Non-human primates

---

[*]Correspondence to: Systems Neuroscience Center, University of Pittsburgh, 4069 BST-3, 3501 Fifth Ave., Pittsburgh, PA 15261, USA. omar@pitt.edu (O.A. Gharbawie).

Competing interest statement
No competing interests.

CRediT authorship contribution statement
NSC & OAG designed and performed experiments, analyzed data, and wrote the manuscript. NSC prepared all figures. OAG obtained funding.

Appendix A. Supporting information
Supplementary data associated with this article can be found in the online version at doi:10.1016/j.pneurobio.2022.102263.

1. Introduction

Spontaneous brain activity, or resting state (RS), provides a window into the organization of brain networks (Bullmore and Sporns, 2009). RS is sampled from minutes-long recordings of electrophysiological or hemodynamic signals that are typically acquired from the whole brain. Statistical dependencies in the recorded time series are then used to generate inferences about functional connectivity (FC) and more broadly about network organization. The capacity for imaging the entire brain non-invasively has propelled fMRI to the forefront of tools used in the acquisition of RS in both humans and animals (Fox and Raichle, 2007; Hutchison and Everling, 2012; Buckner et al., 2013). Resting state fMRI (RS-fMRI) now serves a range of interests from basic research (e.g., cross-species comparisons of brain networks) to fingerprinting brain pathophysiology (e.g., dementia and autism).

RS-fMRI generally operates on a macroscale (e.g., cortical region). With the exception of some recent work (Huber et al., 2017; Shi et al., 2017), the contrast and spatial specificity achieved in RS-fMRI obscure granular details of cortical architecture. This is notably different from the finer scale (e.g., cortical columns and layers) reported in fMRI of stimulus-evoked activity (Kim et al., 2000; Chen et al., 2013). Discrepancy between the effective resolution in the two fMRI paradigms could be related to differences in imaging protocols. Alternatively, it could reflect inherent limitations on the level of detail that can be extracted from correlating RS time series. These points can be adjudicated with optical imaging methods as they provide the signal-to-noise ratio and spatial resolution needed to map distributed cortical networks in fine detail.

Intrinsic signal optical imaging (ISOI) is an attractive candidate for optical recording of RS. ISOI measures hemodynamic response and is therefore operationally similar to fMRI (Grinvald et al., 2000). Findings from resting state ISOI (RS-ISOI) would therefore translate well to the much more widely used RS-fMRI. Even though information on cortical layers cannot be retrieved from ISOI, the method is sensitive to the columnar architecture of cortex. This feature is evident for stimulus-evoked activity in sensory cortex. For example, the columnar organization of visual cortex is captured with outstanding fidelity in ocular dominance and orientation preference maps obtained with ISOI (Bonhoeffer and Grinvald, 1991; Lu and Roe, 2007). The spatial precision of these two-dimensional maps suggests that ISOI has the potential to report FC at high resolution, which would serve many needs. For example, high resolution FC maps would improve site targeting for electrophysiological recordings and perturbations, refine interrogation of cortical rewiring, and create opportunities for addressing long-standing questions about correspondence between FC and anatomical connectivity (Hagmann et al., 2008; Greicius et al., 2009; Heuvel et al., 2009; Honey et al., 2009; Adachi et al., 2012).

Our objective here was to evaluate whether RS-ISOI can report cortical connectivity at columnar granularity. To that end, we benchmarked RS-ISOI against methods that are well-established for revealing cortical connectivity at the desired columnar resolution or better. Specifically, we compared FC maps from RS-ISOI to anatomically traced cortical connections and to microstimulation-evoked activation as measured with ISOI. We conducted our study in sensorimotor cortex of squirrel monkeys where we could use microelectrode mapping to identify cortical areas (i.e., cytoarchitecture) and somatotopy. We then leveraged the cortical parcellation in guiding seed placement and in quantifying connectivity maps. Near-perfect correspondence between FC maps and the benchmark connectivity maps showed that granular details of network organization are embedded in RS.

2. Materials and methods

2.1. Animals

Experiments were performed on 2 adult male squirrel monkeys (*Saimiri boliviensis*). Animals were 4 years old and weighed between 800 and 1200 g. All procedures were approved by the University of Pittsburgh Institutional Animal Care and Use Committee and followed the guidelines of the National Institutes of Health guide for the care and use of laboratory animals.

2.2. Surgical procedures

All procedures and data acquisition were conducted under anesthesia (Table 1). Thirty minutes before sedation, animals were treated with an antiemetic (Zofran, 0.3 mg/kg, IM) and Atropine (0.03 mg/kg, IM) to reduce secretions. Ketamine induction (10–15 mg/kg, IM) was followed with isoflurane (0.5–2.5%) in O_2 (2–3 L/min). Once sedated, Dexamethasone (1 mg/kg, IM), Ketofen (2 mg/kg, IM), and Gentamicin (2 mg/kg, IM) were administered to prevent brain swelling, pain, and infection, respectively. Animals were intubated, artificially ventilated, wrapped in a heating blanket, and secured in a stereotaxic frame. Fluids (5% dextrose in Lactated Ringer’s solution, 2–3 ml/kg/hr, IV) were provided continuously. Heart rate, arterial oxygen saturation, expired CO_2, blood glucose, and body temperature were monitored.

A scalp incision was performed for each procedure. All steps from this point were conducted with the aid of a surgical microscope. In the first procedure for each animal, a rectangular window was opened in the skull over frontal and parietal cortex (~25 × 20 mm, Fig. 1G). That window was accessed in multiple subsequent procedures. After a durotomy, cortical pulsations were stabilized with 3% agarose (Invitrogen, Carlsbad, CA) solution in physiological saline. Data acquisition proceeded from this point and lasted for several hours. The agar was removed at the conclusion of data acquisition and an artificial dura (Tecoflex EG-85 resin, Sakas et al., 1990) was secured into the cranial opening to protect the exposed cortex. The craniotomy was then sealed with dental cement and the scalp was sutured closed. The animal was recovered from anesthesia and another dose of the pre-procedure drugs was administered in addition to Vitamin B12 (0.5 mg/kg, IM). Analgesics and corticosteroids were administered every 12 h for the following 72 h. Survival procedures lasted ~14 h from sedation to alertness and terminal procedures lasted ~24 h.

2.3. Monitoring animal state with EEG

Electroencephalogram (EEG) signals were recorded for monitoring animal state. Stainless steel wires (3 strand, 102 μm diameter, AM systems, Sequim, WA) were inserted into bilateral burr holes near the frontal pole and then secured with dental cement. Wires were removed at the conclusion of each procedure. The voltage differential between the two leads was amplified (10,000x), bandpass filtered (1–500 Hz), and notch filtered (60 Hz) using an AC Amplifier (Model 2800, AM Systems, Sequim, WA). The filtered signal was visualized on an oscilloscope, digitized (1000 Hz, NI USB-6008, National Instruments, Austin, TX), and recorded in MATLAB. Spectrograms and power spectra of the EEG were examined in MATALB (*spectrogram* and *FFT* functions).

Three animal states were classified from temporal and spectral qualities of the EEG. (1) *Light sedation* (0.5–1.5% isoflurane) consisted of slow waveforms; suppression was present in 0–2.0% of the recording. (2) *Semi-deep sedation* (1.75–2.0% isoflurane) consisted of slow waveforms with periodic suppression in 2.0–95.0% of the recording. (3) *Deep sedation* (2.0–2.25% isoflurane) consisted of suppression in >95.0% of the recording. Most ISOI recordings were in the *light* state.

2.4. Motor mapping

We used intracortical microsimulation (ICMS) to map the somatotopic organization of primary motor cortex (M1) and premotor cortex (Fig. 1A–B). A hydraulic microdrive (Narishige MO-10, Amityville, NY) connected to a Kopf micromanipulator (Tajunga, CA) was used for positioning a platinum/iridium microelectrode (125 μm shaft, 300 kΩ median impedance, MicroProbes, Gaithersburg, MD). Each penetration targeted layer V (1800 μm deep) to deliver microstimulation trains (18 cathodal pulses, 0.2 ms pulse width, 300 Hz pulse frequency, 1 Hz train frequency) from an 8-channel stimulator (model 3800, AM Systems, Sequim, WA). Current amplitude was adjusted with a stimulus isolation unit (model BSI-2A, BAK Electronics, Umatilla, FL) until a movement was evoked and up to a maximum of 150 μA. Threshold for a site was the minimum current amplitude that evoked movement on ~50% of microstimulation trains. Combining ketamine infusion (3–6 mg/kg/hr) with low doses of isoflurane (<0.5%) was central to maintaining a state in which ICMS reliably evoked movements.

Two to three experimenters evaluated the evoked movements. Only one experimenter was not blind to the microelectrode location. Each ICMS site was classified according to joint (digit, elbow, etc.) and movement type (e.g., flexion, extension, etc.) that showed the most robust effect at the lowest current amplitude. Mapping was completed over several procedures (30–60 ICMS sites/procedure). Distance between ICMS sites was typically <1 mm. Sites were recorded on a high-resolution photo of cortex. Color coded maps were generated in MATLAB using a Voronoi diagram (*voronoi* function) constrained to 1.0 mm radius per site. Rostral and caudal M1 borders were estimated from current thresholds (≥80 μA), distance from central sulcus, and in relation to area 3a (described next).

2.5. Somatosensory mapping

We recorded multi-unit activity to map the somatotopic organization of somatosensory cortex (Fig. 1C–D). A tungsten or a platinum/iridium microelectrode (125 μm shaft, 420 kΩ median impedance) was lowered to layer IV (700–800 μm deep). Distance between sites was typically <1 mm. Signal was amplified (10,000x) and filtered (bandpass 300–5000 Hz, notch 60 Hz) using an AC amplifier (Model 2800, AM Systems, Sequim, WA). The signal was then passed through a 50/60 Hz noise eliminator (HumBug, Quest Scientific Instruments Inc., Vancouver, BC) and monitored with an oscilloscope and a loudspeaker. Receptive fields were determined from neural responses to stimulation of the contralateral body. Responses were classified as cutaneous or proprioceptive. Units in areas 3b and 1 responded to cutaneous stimulation and had relatively small receptive fields (e.g., single digit phalanx). In contrast, units in area 3a were unresponsive to skin contact and responded only weakly to the manipulation of multiple joints (e.g., entire digit or multiple digits). Area 2 contained a mixture of units that responded to joint manipulation or cutaneous stimulation. Cortical borders were estimated from transitions in receptive field properties along the rostro-caudal dimension (Sur et al., 1982). Somatosensory maps were generated with Voronoi diagrams as described above.

2.6. Intrinsic signal optical imaging

We used intrinsic signal optical imaging (ISOI) to measure resting state (RS) and ICMS-evoked activation. Images of cortex were acquired with a camera (Photon Focus, Lachen, Switzerland) based on a 12-bit CMOS sensor (1312 × 1082 pixels). An optical imaging system (Imager 3001, Optical Imaging Ltd, Rehovot, Israel) controlled image acquisition. The tandem lens combination provided a field-of-view (~26 × 22 mm; ~19 μm/pixel) that included the microelectrode mapping territory as well as 2–3 mm of skull around the perimeter. Camera angles were adjusted with a 3-axis geared head (410 Junior Geared Tripod Head, Manfrotto, Cassola, Italy). Camera position (x, y, and z directions) was translated with independent linear stages. For spatial reference, blood vessel patterns were imaged (528 nm illumination) at the start of each ISOI recording. Three independently controlled LEDs (620 nm) provided illumination during ISOI.

2.7. Resting state

2.7.1. Image acquisition and processing—

Spontaneous cortical activity was recorded with ISOI for 15 min. Frames were temporally binned to 10 Hz. The raw time course and power spectrum for the entire field-of-view (FOV) was examined for initial assessment of image quality. Segments of data were excluded if there was evidence of artifact, which was typically due to illumination instability, animal state fluctuations, or setup vibrations. The remaining frames were spatially binned by a factor of 3 (from ~19 μm/pixel to ~58 μm/pixel).

Image processing was conducted in both the temporal and spatial domains using MATLAB scripts. (1) Frames were temporally binned from 10 Hz to 2 Hz for de-noising and to speed up computation in subsequent steps. (2) A moving median filter (2 s window) smoothed the time course of each pixel to minimize noise. (3) First-frame subtraction converted pixel values to reflectance change (ΔR/R%) from baseline. (4) A high-pass filter (Butterworth, 3rd order, cutoff 0.005 Hz) was applied to each pixel to minimize the effects of illumination drift. (5) Multiple linear regression was used to remove nuisance signals from the time course of each pixel. This step minimized the effects of global signals, blood vessel activity, and residual artifact. The most effective regressors were groups of pixels that overlapped the skull or major blood vessels. To identify those pixels, principal component analysis (PCA) and k-means clustering were iteratively applied until we accounted for 85–90% of the variance in pixel values overlapping skull and blood vessels. This was achieved with 5–6 clusters of pixels over the skull and 5–6 clusters of pixels over major blood vessels. For each cluster, the average time course of all pixels was used as a regressor in the multiple linear regression. The average time course for all visible cortex was used as an additional regressor, which is similar to global signal regression in RS-fMRI (Murphy and Fox, 2017). (6) Frames were then spatially filtered for smoothing (gaussian kernel = 2 pixels or 120 μm radius). (7) Each time course was bandpass filtered (Butterworth, 3rd order, 0.01–0.10 Hz) to hone in on infra-slow signals (Cordes et al., 2001). The effects of each processing step are shown for representative sites (Supp. Figs. 1–2).

2.7.2. Functional connectivity maps—Functional connectivity (FC) was measured from seeds in individual ISOI recordings. A seed (radius = 4 pixels, ~232 μm) was defined as a cluster of pixels. The time courses of those pixels were averaged with weighting towards the center (Gaussian, sigma = 0.5) to generate one time course for the seed. The seed time course was correlated (Pearson) with time courses of all other pixels. Coefficients were then regressed as a function of distance from the seed to correct for the effect of distance on correlation strength. Pixels were color coded according to coefficient values to generate an FC map. This process was repeated for every seed available in the FOV and for every ISOI recording (Table 1). FC maps from the same hemisphere and seed were co-registered (details in *common reference registration*) and then averaged for de-noising. Pixels were flagged if their coefficients had a distribution >zero (unpaired t-test, $p < 0.001$). The statistical analysis was applied only to pixels that were present in ≥10 recordings. Average FC maps were thresholded by excluding non-flagged pixels.

2.8. ICMS-evoked activation

2.8.1. Image acquisition and processing—ISOI was used to measure ICMS-evoked activation from select cortical sites. Procedure details were previously described (Card and Gharbawie, 2020). A microelectrode (platinum/iridium, 125 μm shaft) was lowered 1000 μm below the cortical surface. Each site was tested on ≥50 blocks; one ICMS trial and one Blank trial (i.e., no ICMS) per block. Image acquisition was 4 s/trial followed by 12-second inter-trial interval. Frames were temporally binned to 5 Hz. The stimulation train consisted of 150 biphasic pulses, 0.2 ms phase width, 300 Hz pulse frequency, and 60 μA current amplitude. Microelectrode impedance was comparable at the start (median = 240 kΩ) and end of each experiment (median = 320 kΩ). Microstimulation parameters were based on a systematic investigation of the effects of train duration, frequency, pulse amplitude, and electrode depth on ICMS-evoked activation (figure 9 in Card and Gharbawie, 2020). With the exception of the relatively low current amplitude used here, the present microstimulation parameters were consistent with other studies that measured the ICMS-evoked response with ISOI (Stepniewska et al., 2011; Friedman et al., 2020a), or with fMRI (Tolias et al., 2005; Ekstrom et al., 2008; Moeller et al., 2008; Klink et al., 2021), or from movement classification (Graziano et al., 2002; Stepniewska et al., 2005; Baldwin et al., 2016).

ISOI data was processed and analyzed using custom MATLAB scripts. Two image subtractions were applied to minimize global signals. (1) In every trial, the first data frame was subtracted from subsequent frames. (2) In every block of trials, frames of the Blank condition were subtracted from frames of the ICMS condition. Next, 2–3 data frames from ICMS minus Blank (1000–1600 ms from stimulation onset) were averaged for every trial. Those mean frames were then used for generating average subtraction maps. Maps were spatially filtered to correct uneven illumination (high-pass median filter, kernel = 250–350 pixels or 5–7 mm) and for smoothing (low-pass Gaussian filter, kernel = 10 pixels or 190 μm). To enhance contrast, the distribution of pixel values was clipped (median ± 1.5 SD). In the final subtraction maps, dark pixels indicated reflectance change due to oximetry modulations from local increases in neural activity. Dark pixels therefore reported ICMS-evoked activation.

2.8.2. Effective connectivity maps—Mean frames from ICMS trials were compared on a pixel-by-pixel basis to mean frames from Blank trials (paired t-test). Pixels that darkened (left tail, $p < 0.001$) in response to ICMS were included in EC maps.

2.9. Anatomical connectivity

2.9.1. Tracer injections—Retrograde and anterograde tracers were injected in cortical sites to examine their anatomical connectivity (AC). Injections were in a subset of sites in M1, PMd, and PMv that had been investigated with ICMS+ISOI. Tracers were pressure injected using Hamilton syringes fitted with a beveled glass pipette. For each site, tracer was injected 700 μm and 1400 μm below the cortical surface. Four tracers were used: (1) Cholera toxin B subunit (CTB, SigmaMillipore). (2) Biotinylated dextran amine 1:1 mixture of 3,000 MW and 10,000 MW (BDA, ThermoFisher Scientific). (3) Dextran tetramethylrhodamine 3,000 MW, commonly known as fluoro ruby (FR, ThermoFisher Scientific). (4) Fast blue (FB, Polysciences). Total volumes were 0.4 μL for FB (2% in dH_2O), 0.8 μL for FR (10% in dH_2O), 0.6 μL for CTB (1% in dH_2O), and 0.8–1.5 μL for BDA (10% in dH_2O). After 12–13 days of tracer transport, a terminal experiment was conducted for additional ISOI recordings and microelectrode mapping. Also, microlesions were made (5 μA DC) to create salient landmarks for co-registering histological sections, ISOI maps, and microelectrode maps.

2.9.2. Histology—After a lethal dose of sodium pentobarbital (Fatal Plus, Vortech), intracardial perfusion proceeded with PBS (pH 7.4), followed by 2% paraformaldehyde in PBS, and then 2% paraformaldehyde in PBS with 10% sucrose solution. Cortex was separated, flattened, and blocked >5 mm beyond the imaging FOV. Two glass slides held the cortex flat during fixation (4% paraformaldehyde, ~24 h) and cryoprotection (30% sucrose, ~48 h). Cortex was then cut parallel to the surface and sections (50 μm) were stored in series. One series was reacted in a nickel-intensified DAB (diaminobenzidine dihydrochloride) to visualize BDA labeling. A separate series was reacted for CTB immunohistochemistry and labeled cells were visualized with a nickel-intensified DAB reaction (Bruce and Grofova, 1992). A DAB and alkaline phosphate reaction was carried out in the same series to visualize BDA labeling. A third series was mounted onto slides without processing for examination of fluorescent labeling.

2.9.3. Section plotting—Sections were examined with a microscope (Eclipse E600, Nikon, Minato City, Tokyo, Japan) outfitted with a motorized stage and x,y encoder

(MAC5000 PS-SYSTEM 73005020, Ludl Electronic Products, Hawthorne, NY). FR-labeled cells were visualized with fluorescence illumination passed through a TRITC HYQ filter (excitation: 530–560 nm, emission: 590–650 nm) and FB-labeled cells with a UV-2E/C filter (excitation: 340–380 nm, emission: 435–485 nm). BDA-labeled and CTB-labeled cells were visualized with bright-field illumination. Cells and landmarks (microlesions, injection sites, sulci, blood vessels, tissue artifacts) were plotted using Neurolucida software (version 6.0, MBF Bioscience). For each injection, cells were plotted from 4 to 8 sections (>200 μm between sections).

2.9.4. Anatomical connectivity maps—

Neurolucida files were converted into DXF format (AutoCAD version 23.1, Autodesk, San Rafael, CA) with x,y coordinates for plotted cells and landmarks. DXF files were loaded into Adobe Illustrator (Version 25.3, Adobe, San Jose, CA) and then copied into Adobe Photoshop (Version 21.1.0, Adobe, San Jose, CA). Sections from the same injection were co-registered then labeled cells were counted in circular bins (diameter 10–20 pixels, 190–380 μm). Bin diameter increased with distance from the injection site (~8 μm/mm) as a correction step that approximates the distance regression applied in FC maps. Cell counts were summed across corresponding bins and collated into a single section. The value at each bin was expressed as a percentage of the total number of labeled cells to generate an anatomical connectivity (AC) map.

2.10. Common reference registration

The common reference for each hemisphere was a high-resolution, high-contrast image of the cortical blood vessels. Microelectrode penetrations, microlesions, and tracer injections were marked on that image. ISOI frames were co-registered to the common reference using non-linear bicubic transformation for 300–600 points. Co-registration was conducted with a custom MATLAB script and a script from the MATLAB file exchange [B-spline Grid, Image and Point based Registration, Dirk-Jan Kroon, 2021]. Histological sections were co-registered to the common reference using the same approach and the Puppet Warp feature in Adobe Photoshop (Version 21.1.0, Adobe, San Jose, CA).

2.11. Statistical analyses

Statistical tests were performed using SPSS and MATLAB. Parametric tests were used wherever assumptions about the distribution were satisfied (e.g., normality and homoscedasticity). Normality was tested using the Kolmogorov–Smirnov test and homoscedasticity was tested using Levene's test. Non-parametric tests were used if assumptions were not satisfied. For one- or two-sample comparisons, either a t-test or a Wilcoxon rank-sum test was performed. For comparisons across >2 parametric populations, a one-way ANOVA was used with a post hoc Tukey's HSD test. For comparisons across >2 non-parametric populations, a Kruskal-Wallis test was performed with a post hoc Dunn's test. For all tests, a significance level of $\alpha = 0.05$ was used. Bonferroni correction was applied where appropriate. Significance conventions in figures: $^{*}p < 0.05$, $^{**}p < 0.01$, $^{***}p < 0.001$.

3. Results

We recorded resting state with intrinsic signal optical imaging (RS-SOI) and compared the functional connectivity (FC) against well-established benchmarks of cortical architecture. RS-ISOI was recorded in monthly experiments conducted over ~1.5 years (e.g., video 1). Our testbed was the squirrel monkey sensorimotor cortex where we could rely on microelectrode mapping for comprehensive cortical parcellation. We generated functional connectivity (FC) maps for seeds throughout the FOV. In the same sites, we also mapped (1) *effective connectivity* (EC) using intracortical microstimulation + ISOI and (2) *anatomical connectivity* (AC) using tracer injections. Quantitative comparisons showed excellent correspondence between FC maps, EC maps, and AC maps.

Supplementary material related to this article can be found online at doi:10.1016/j.pneurobio.2022.102263.

3.1. Consistent cortical parcellation with microelectrode mapping

We used high density microelectrode mapping (<1 mm between sites) to define cortical borders and somatotopy in motor and somatosensory cortex. The somatotopy of motor (Fig. 1A–B) and somatosensory (Fig. 1C–D) maps was consistent between monkeys and followed a medial-lateral organization (leg to face) that is well-established for New World monkeys (Welker et al., 1957; Merzenich et al., 1978; Gould et al., 1986; Padberg et al., 2005; Mayer et al., 2019). Criteria for estimating cortical borders included current thresholds, receptive field properties, and distance to central sulcus.

The forelimb representation occupied most of the motor territory. Within the M1 forelimb representation, hand zones (digit and wrist) were surrounded by arm zones (elbow and shoulder), which is consistent with previous work (Dancause et al., 2008; Card and Gharbawie, 2020). PMv and PMd contained independent hand zones (Fig. 1A–B) and the PMd hand zone was surrounded by an arm zone. Motor and somatosensory maps were merged into a single map (Fig. 1E–F). We used the amalgamated maps to parcellate cortex, place seeds, and quantify connectivity maps. The size of the responsive cortical territory was similar between animals (monkey R = 236.7 mm^2 & monkey B = 221.4 mm^2). Zones in the middle of the map (i.e., hand, arm, and trunk zones) were consistent in size between animals, whereas zones on the perimeter (i.e., leg, tail, face) were more variable (Fig. 1H). Discrepancy between middle and perimeter was likely related to the extent of microelectrode mapping as opposed to differences between animals.

To assess map stability, a subset of sites was retested months after initial classification. Each retest occurred < 250 μm from the original site. Most of the retested motor sites (32/37 sites, 86.5%) had the same classification at both time points (267 ± 151 days apart, 193 ± 55 μm apart, mean ± SD). Similarly, most of the retested somatosensory sites (12/14 sites, 85.7%) had the same classification at both time points (189 ± 118 days apart, 195 ± 53 μm apart, mean ± SD). This sample of retested sites (5.7% of total sites) confirmed that maps were stable enough for reliable cortical parcellation.

3.2. Measuring functional connectivity from RS-ISOI

In a representative RS-ISOI recording (video 1), we placed the seed in the PMv hand zone (Fig. 2A, blue circle, 232 μm radius). We targeted this zone because its connections include nearby, tightly spaced patches in M1 and PMd, as well as 1 or more distant patches in area 2. We considered this constellation of patches a high benchmark for evaluating RS-ISOI in mapping connectivity. For initial inspection of the site, signals were processed in the spatial and temporal domains (Fig. 2B top vs bottom; Supp. Fig. 1 & Fig. 2). Then we flagged frames in which reflectance change at the seed darkened ≥1.5 SD beyond the mean value of the time course (Fig. 2B bottom, red line). Averaging flagged frames revealed dark patches in M1, PMd, 3a, 2, and at the seed in PMv (Fig. 2C arrowheads). The locations and sizes of the patches were consistent with cortical connections from tracer studies (Dum and Strick, 2005; Dancause et al., 2006b; Stepniewska et al., 2006; Gharbawie et al., 2011b; Hamadjida et al., 2016). Thus, credible reports on cortical connectivity can be extracted from RS-ISOI time series.

To quantify co-fluctuations in the time series, we conducted pairwise correlations (Pearson) between the seed time course and the time courses of all other pixels. The map of correlation coefficients had hot spots (Fig. 2D) that were in the same locations as the dark patches in Fig. 2C. We compared time courses from 3 regions-of-interest (ROI) with the seed time course (Fig. 2D, colored circles). (1) Coupling between the time courses from the red ROI and the seed was confirmed with tight positive correlation ($\rho = 0.67$, Fig. 2E–F top). (2) Time courses from the orange ROI and the seed had no discernible relationship ($\rho = 0.02$, Fig. 2E–F middle). (3) Time courses from the green ROI and the seed were consistently out of phase, which was confirmed with strong negative correlation ($\rho = -0.53$, Fig. 2E–F bottom). Similar observations are in Video 2.

Supplementary material related to this article can be found online at doi:10.1016/j.pneurobio.2022.102263.

Next, we investigated the optimal duration for recording RS-ISOI. FC quality and stability improves with imaging duration (Birn et al., 2013), but the gain is at the expense of processing time due to computational overhead. This motivated us to find the point at which gains from imaging duration begin to diminish. To that end, we acquired RS-ISOI for 30 min in 4 separate recordings (2 recordings/animal). Each recording was segmented according to 16 different durations. For example, 30 × 1-min segments, 15 × 2-min segments, 10 × 3-min segments, etc. Seeds were then systematically placed throughout the FOV (Fig. 3A) to generate FC maps from each segment. Maps from equal segments were directly compared to one another (Pearson correlation). For example, a map from a 1-min segment would have been compared to 29 maps from the remaining 1-min segments. Fig. 2G shows representative comparisons (top vs. bottom). Correspondence between FC maps improved with segment duration, which was confirmed with higher correlation coefficients. Comparisons from all seeds and imaging runs indicated that FC maps from the 15-min segments were robust ($\rho = 0.80$, Fig. 2H). Correspondence between FC maps decreased ($\rho = 0.73$) in the 10-min segments, but the drop was more substantial for shorter segments ($\rho = 0.59$ at 5 min; $\rho = 0.38$ at 2 min; $\rho = 0.15$ at 0.5 min). We therefore considered 15-min the optimal duration and used it as the standard in all subsequent RS-ISOI recordings, which was consistent with previous RS-ISOI recordings (White et al., 2011; Vasireddi et al., 2016).

3.3. Functional connectivity is consistent across months

Our next objective was to evaluate FC map consistency across ISOI recordings (14–16 months apart). We generated FC maps for each recording from a grid of seeds (Fig. 3A; 1 map/seed/recording) and then conducted 3 sets of pairwise correlations (Pearson) between maps. (1) Comparisons ($n = 68{,}062$) in matched sites indicated variation in FC maps across recordings ($\rho = 0.49 \pm 0.21$). Nevertheless, after thresholding each map to coefficients ≥0.25≥ 0.25 and redoing the comparisons, it was evident that FC maps were in fact consistent across recordings ($\rho = 0.80 \pm 0.13$). For reference, we found no correspondence ($\rho = 0.02 \pm 0.32$) between FC maps from non-matched sites ($n = 1{,}483{,}451$ comparisons). Thus, thresholded FC maps were spatially specific and consistent across months of recordings.

We reasoned from these results that averaging FC maps from the same seed could be an effective denoising step. Indeed, the effect of averaging was evident in a side-by-side comparison of an FC map from 1 recording and an FC map averaged from 13 recordings (Fig. 3B–C). Seed (white dot) location in PMv matched Fig. 2. Pixels with high coefficients (orange-red) were consistent in the individual and average FC maps. In contrast, pixels with low coefficients (white-yellow) occupied more territory in the individual FC map. These observations confirmed that the relatively strong features of an FC map were stable over time.

Observations from Fig. 3A–C motivated us to average and threshold FC maps. For thresholding, we included only pixels with coefficient distributions >zero (one-tailed t-test, $p < 0.001$) in order to exclude noisy pixels and low-coefficient pixels. As expected, averaging and thresholding the map in Fig. 3B resulted in a cleaner iteration (Fig. 3D) that was also consistent between animals (Fig. 3E). For context, we superimposed cortical borders and shaded in the hand (green) and arm (blue) zones. In both animals, significant pixels were concentrated in hand zones and to a much lesser extent in arm zones. Only a small fraction of significant pixels was outside of the forelimb zones. Beyond the seed location in PMv, significant pixels were most concentrated in M1, 3a, and area 2. Pixels were sparse and had weaker coefficients in PMd, area 3b, and area 1. Fig. 3F summarizes the connectivity profiles in Fig. 3D–E. To simplify the plots, cortical areas were grouped by modality: (1) motor (M1, PMd, PMv), (2) somatosensory (areas 3a, 3b, 1, and 2), and (3) area 5. FC quantification relative to functional zone (e.g., motor hand) was based on the number of significant pixels and their coefficients. As expected from Fig. 3D–E, the polar plot showed that FC was stronger with hand zones than with arm zones. FC was also stronger with motor fields than with somatosensory fields. Finally, cosine similarity (CS, detailed below) confirmed that the FC profile for this site was consistent between animals (CS = 0.94).

We also tested the effects of averaging and thresholding on an FC map of a completely different profile. Seeds were placed in the representation of digit 2 in area 3b (Fig. 3G–H). Most significant pixels were in hand zones, which was apparent in the polar plot. Those pixels were concentrated in somatosensory areas 3b, 1, and to a lesser extent in areas 3a and 2. Beyond somatosensory cortex, significant pixels were present in M1 hand and PMv hand, but to different extents between animals. The overall distribution of significant pixels was consistent between animals (CS = 0.99) and with previous tracer injections into digit representations in areas 3b and 1 (Liao et al., 2013; Négyessy et al., 2013). Thus, our FC maps for PMv and area 3b indicate that averaging and thresholding reveals connectivity patterns that are consistent between animals and with known anatomical connections. Averaging and thresholding were therefore implemented in all subsequent analyses.

3.4. Functional connectivity corresponds with effective connectivity

Our next objective was to benchmark FC against ICMS-evoked activation [i.e., effective connectivity (EC)], which was a surrogate here for stimulus-driven activity and for anatomical connectivity. ICMS afforded us control over stimulus parameters and the capacity to test many sites. We evaluated correspondence between FC and EC maps on three metrics: (1) Cosine similarity (CS) measures the extent to which both maps overlap the same functional zones. CS ranges from 0 to 1 (no similarity to perfect similarity). (2) Mean separation (MS) measures the average distance between pixels in both map. Low MS indicates high spatial coincidence between maps. (3) Goodness of fit (GOF) combines CS and MS (Eqs. (1) & (2)). MS is first normalized by the *max* separation recorded (i.e., worst) between any pair of maps *i*. GOF ranges from 0 to 1 (perfect similarity to no similarity).

$$MS_{norm,\,i} = \frac{MS_i}{MS_{max}} \tag{1}$$

$$GOF_i = \frac{1 - CS_i + MS_{norm,\,i}}{2} \tag{2}$$

We compared FC and EC maps in two representative sites (Fig. 4A–H). In one site (Fig. 4A, white dot), the stimulating microelectrode was in the same PMv location as Fig. 2 & Fig. 3. The average optical image showed that ICMS activated a main patch around the microelectrode and smaller patches in M1, PMd, and areas 3a and 2 (Fig. 4A, arrowheads). To generate an EC map, we flagged pixels that darkened significantly in the ICMS condition as compared to the blank condition (t-test, $p < 0.001$). Significant pixels were then ranked according to their ΔR/R values (Fig. 4B). The same scale was applied to the average FC map from the same site (Fig. 4C). The FC map was also thresholded at several cutoffs (min $p < 10^{-1}$, max $p < 10^{-7}$) and we selected the one that achieved the best GOF with the EC map. Correspondence between FC and EC maps was apparent in the side-by-side comparison (Fig. 4B–C) and in the polar plot (Fig. 4D). The three metrics of overlap (CS = 0.99; MS = 0.04 mm; GOF = 0.01) showed a near-perfect fit between FC and EC maps for this site. In another site, the microelectrode was in area 1 arm zone (Fig. 4E, white dot). Correspondence between FC and EC was apparent in the maps (Fig. 4F–G) and polar plot (Fig. 4H). The three metrics of overlap (CS = 0.97; MS = 0.06 mm; GOF = 0.03) confirmed the fit between FC and EC maps. Thus, observations from two sites indicated that FC maps overlapped exceptionally well with EC maps.

We expanded comparisons between FC and EC maps to 48 sites across monkeys (Fig. 4I–J). We compared FC and EC maps from matched sites and from non-matched sites. CS values were highest (i.e., best) for matched sites and decreased with differences in site identity (Fig. 4K). Site pair category had an effect on CS values (Fig. 4K, Kruskal-Wallis test, H(3) = 484.43, $p < 0.001$) and pair categories differed from one another (Dunn's test, $p < 0.001$). Similarly, MS values were lowest (i.e., best) for matched pairs and increased with differences in site identity (Fig. 4L). Pair category had an effect on MS values (Fig. 4L, Kruskal-Wallis test, H(3) = 375.38, $p < 0.001$) and pair categories differed from one another (Dunn's test, $p < 0.001$). The effects in CS and MS were also evident in the GOF (Fig. 4M, Kruskal-Wallis test, H(3) = 512.55, $p < 0.001$). Our observations indicate that correspondence was high between FC and EC maps. Moreover, lack of overlap between maps from non-matching sites suggests that somatotopy was a governing factor of the connectivity, which is consistent with previous reports on the FC of the "somatomotor network" (Yeo et al., 2011; Thomas et al., 2021).

The main patch that surrounded each site accounted for ~50% of significant pixels in FC and EC maps (Fig. 4N). This motivated us to examine whether correspondence between FC and EC maps was skewed by overlap in the main patch in both maps. We therefore excluded pixels within 2 mm of each site, which effectively removed the main patch in most sites. We then repeated the comparisons between FC and EC maps (Fig. 4O). Excluding the main patch had no effect on the statistical relationships observed in Fig. 4M, which points to universal overlap between FC and EC maps as opposed to heavy weighting in the main patch. The results in Fig. 4 showed that FC maps reliably reported the spatial organization and strength of site connectivity.

3.5. Mapping anatomical connectivity with tracer injections

Our next objective was to benchmark FC against AC revealed with tracers. We also compared EC to AC to calibrate our assumptions about using EC as a surrogate for AC. First we review results from the tracer injections (n = 5; Fig. 5A & G) and affiliate AC maps. M1 (n = 2) and PMd (n = 2) injections were in arm zones and were in similar locations in both animals. The PMv injection was in the hand zone. After tracer transport, cortex was flattened and cut tangentially to facilitate co-registration with the common reference. Injection sites were apparent from tissue artifact and tracer uptake (e.g., Fig. 5B). For every section, the locations of labeled cells (e.g., Fig. 5C) and landmarks were plotted. Sections were collated (e.g., Fig. 5D, n = 8 sections) then converted into a heat map (Fig. 5E), which is considered the AC map. For a BDA injection in caudal M1, the AC map showed that most labeled cells were concentrated in M1 followed by areas 3a, 1, 2, and PMd (Fig. 5E). Most labeled cells were in arm zones (blue shade). Cells in hand zones were primarily in M1. Quantification of the heat map indicated that >60% of labeled cells were in arm zones and only ~20% of labeled cells were in hand zones (Fig. 5F). This connectivity profile was confirmed in the second animal with a FR injection into the M1 arm zone (Fig. 5H–I). The higher proportion of cells labeled in trunk zones was likely due to the relatively medial location of the present injection as compared to the first M1 injection (Fig. 5A).

Connectivity profiles for PMd and PMv were distinct from those of M1. For example, CTB injection in PMd (Fig. 5G) labeled cells in PMd, M1, and PMv (Fig. 5J). Somatosensory areas 3a and 3b were almost devoid of labeled cells, but areas 1 and 2 contained small patches of labeled cells. More labeled cells were in area 5 than in anterior parietal cortex. Cells in motor areas were distributed equally between arm and hand zones (Fig. 5K). In contrast, cells in parietal cortex were in arm zones only. This connectivity profile was confirmed in the second animal (Fig. 5A, FB). The main difference was that the second injection (Fig. 6A–B) labeled more cells in area 3a and fewer cells in areas 1 and 2. Finally, BDA injection in PMv (Fig. 5G) labeled cells in PMv, M1, and PMd (Fig. 6G–H). Cells in parietal cortex were in areas 3a, 2, and 5. Overall, most cells were in hand zones. M1 contained the smaller proportion of cells that were in arm zones. The connectivity profiles observed here for M1, PMd and PMv were consistent with previous reports in New World monkeys (Dum and Strick, 2005; Dancause et al., 2006a, 2006b; Stepniewska et al., 2006; Gharbawie et al., 2011a). The present AC maps are therefore reliable benchmarks for comparing FC and EC maps.

3.6. Functional and effective connectivity correspond with anatomical connectivity

For each tracer injection site, we compared FC and EC maps with AC maps. In two representative sites (Fig. 6A–L), correspondence was evident between the three maps and polar plots. The three overlap metrics indicated high correspondence between FC and AC maps from matched sites (Fig. 6M). For reference, the same metrics indicated poor overlap between FC maps and AC maps from non-matched sites (Fig. 6M). A two-sample t-test confirmed that overlap values were better for matched pairs than for non-matched pairs; CS: $t(11) = -4.62$, $p < 0.001$; MS: $t(11) = 3.92$, $p < 0.001$; GOF: $t(11) = 4.52$, $p < 0.001$. Similarly, overlap metrics for EC and AC maps were better for matched sites than for non-matched sites (Fig. 6N; CS: $t(11) = -5.04$, $p < 0.001$; MS: $t(11) = 4.98$, $p < 0.001$; GOF: $t(11) = 5.37$, $p < 0.001$). Thus, Fig. 6 shows that RS-ISOI and ICMS+ISOI both reveal cortical connectivity with the same reliability and accuracy as tracer injections.

3.7. Animal state affects functional connectivity

FC is successfully mapped under anesthesia (Vincent et al., 2007; Mohajerani et al., 2010; Wang et al., 2013; Hutchison et al., 2014; Hori et al., 2020a). However, FC quality is susceptible to sedation depth (Hori et al., 2020b; Hutchison et al., 2014; Liu et al., 2013a–c). This motivated us to investigate the relationship between animal state as determined from intracranial EEG patterns and FC quality. To that end, we adjusted the isoflurane dosage to achieve 3 distinct states for RS-ISOI recordings. Each state was examined in ≥3 RS-ISOI recordings (Table 2). The average power spectrum from EEG recordings under *deep sedation* indicated that power was attenuated across frequencies (Fig. 7B). In contrast, the power spectrum from *semi-deep sedation* was shifted just below the power spectrum from *light sedation*. Examination of the time series showed that the burst phase in *semi-deep sedation* had a comparable power spectrum to *light sedation*. Thus, periodic suppression drove the downward shift observed in the power spectrum from *semi-deep sedation* (Fig. 7B).

The relationship between sedation depth and FC is illustrated for two representative sites (Fig. 7C–H). Sedation depths were tested in successive recordings in the same experiment. In *light sedation*, FC maps had well-defined patches of high correlations (Fig. 7C & F). Seed placement in the M1 arm zone (Fig. 7C) revealed an FC map that was consistent with the AC map that we reported in Fig. 5E and with previous work (Stepniewska et al., 1993). Similarly, the FC map that we generated for the area 3b digit zone was consistent with the connection patterns of single digit representations (Liao et al., 2013; Négyessy et al., 2013). FC map quality degraded in the other states. In *semi-deep sedation*, patches were less intense and some disappeared altogether (Fig. 7D & G). Nevertheless, the overall patterns were recognizable as weaker versions of Fig. 7C & F. In *deep sedation,* distant patches disappeared completely and FC maps were unrecognizable (Fig. 7E & H). Decay in map quality was transient as the original FC patterns were restored once EEG readings indicated return to *light sedation*. To formalize the relationship between animal state and FC map quality, we quantified correspondence between FC and AC maps at the 5 tracer sites (Fig. 7I). For the *light sedation*, low GOF values and a tight distribution confirmed that those FC maps corresponded well with AC maps. Larger GOF values and wider distributions in the other two states indicated lower correspondence between FC maps and AC maps. These observations motivated us to record RS-ISOI under *light sedation,* defined by the absence of EEG suppression, throughout the study. We note that *light sedation* was achieved with 0.9–1.5% isoflurane in the 9 recordings in this experiment (Table 2). But isoflurane dosing needed to be as low as 0.5% if we consider all 28 recordings from the same state (Table 1).

This experiment also shed light on parameters for monitoring sedation depth. For example, we found no relationship between isoflurane dose and heart rate ($r^2 = 0.09$, Fig. 7J left) and no relationship between heart rate and map quality ($r^2 = 0.01$, Fig. 7K left). In contrast we found a strong relationship between isoflurane dose and EEG suppression ($r^2 = 0.68$, Fig. 7J right) and between EEG suppression and map quality ($r^2 = 0.58$, Fig. 7K right).

4. Discussion

We investigated whether resting state (RS) can reveal granular details of cortical architecture. To that end, we recorded RS with intrinsic signal optical imaging (RS-ISOI) in anesthetized squirrel monkeys. Then we correlated the infra slow signals (0.01–0.10 Hz) to infer functional connectivity (FC) for seeds throughout motor and somatosensory cortex. FC was benchmarked against (1) effective connectivity and (2) anatomical connectivity. High correspondence between the three connectivity modalities showed that spatio-temporal patterns embedded in RS time series, faithfully report cortical connectivity at columnar resolution.

4.1. High resolution FC

RS is typically recorded with fMRI (RS-fMRI, Biswal et al., 1995). The approach is invaluable for insight about the macro-organization of brain networks (Fox and Raichle, 2007; Bullmore and Sporns, 2009). However, it lacks the contrast and spatial resolution needed for revealing fine network features. ISOI shares many of the operational principles of fMRI, but provides higher effective resolution. For example, ISOI typically reports stimulus-evoked activity at columnar scale (Bonhoeffer and Grinvald, 1991; Sheth et al., 2004; Lu and Roe, 2007). Here, we showed that this high effective resolution is conserved in the cortical architecture extracted from RS-ISOI. Even after down sampling, our RS-ISOI data (60 μm/pixel) still had considerably higher spatial resolution (≥10x) and higher contrast than available in most RS-fMRI paradigms. Our findings extend previous RS-ISOI reports (White et al., 2011; Vazquez et al., 2014; Vasireddi et al., 2016; Bauer et al., 2018; Kura et al., 2018) by showing that the approach is effective in monkeys and reveals cortical connectivity at columnar resolution.

Among the strengths of ISOI is that it does not require extrinsic indicators. This feature is particularly useful for imaging large brains (e.g., monkeys). Indicators such as voltage sensitive dyes and GCaMP are used in RS recordings and provide better fidelity to neural activity than ISOI (Arieli et al., 1995; Mohajerani et al., 2013; Chan et al., 2015). But the temporal resolution gain does not necessarily improve the quality of FC for two reasons. First, FC quality is most robust in infra-slow signals < 0.1 Hz (Mayhew et al., 1996; Cordes et al., 2001; Chan et al., 2015; Vanni et al., 2017), which are sufficiently sampled in ISOI and in fMRI. Second, signals recorded in ISOI and fMRI are lagging indicators of the electrophysiological and calcium signals measured in other methods (Logothetis et al., 2001; Devor et al., 2003; Shmuel and Leopold, 2008; Schölvinck et al., 2010; Ma et al., 2016; Shi et al., 2017). Thus, ISOI is perhaps the most versatile and least invasive optical method for recording RS in wild type animals.

4.2. High resolution cortical parcellation

Cortical parcellation was achieved from dense microelectrode mapping that would not have been feasible without the longitudinal approach adopted. By generating an *atlas* for each hemisphere, we minimized the effects of inter-subject variability. We also eliminated distortions that could be expected from co-registering results across our animals or with curated squirrel monkey brains (Schilling et al., 2019). We justified our labor-intensive approach to cortical parcellation with the accuracy afforded for co-registering connectivity maps with anatomical and functional divisions. These provisions ensured that connectivity quantification was both accurate and objective. Moreover, they enabled us to use relatively small seeds (~230 μm diameter), which was in itself important for evaluating the granularity of FC maps.

4.3. FC corresponds with evoked cortical activation

FC patterns are consistent with cortical activation patterns driven by peripheral stimulation or behavioral demand (e.g., Vincent et al., 2007; Mohajerani et al., 2013; Vasireddi et al., 2016). Those observations motivated us to benchmark our FC maps against stimulus driven activation. We compared FC maps from 48 seeds with ICMS-evoked activation maps (ICMS+ISOI) of the same cortical sites in the same subjects. We favored ICMS because it provides control over stimulus location, intensity, and is more effective than peripheral stimulation at driving motor cortical areas. High correspondence between FC and ICMS-evoked activation confirmed the effectiveness of RS-ISOI at revealing fine details of cortical networks.

4.4. FC corresponds with anatomical connectivity

The relationship between FC and anatomical connectivity (AC) has been intensely investigated with several approaches. The general consensus is that strong AC is predictive of FC (Buckner et al., 2013). This principle is instructive for generating hypotheses about functional networks, but it also underscores the limited utility of FC for interrogating AC. Our direct comparisons showed strong correspondence between FC and AC both in terms of spatial organization and connectivity strength. The FC map that we generated for each seed was in effect a faithful projection of monosynaptic, ipsilateral, connections for that site. This observation supports a tight relationship between FC and intra-hemispheric AC, which we would also expect for other cortical networks.

We leveraged ICMS+ISOI to expand comparisons between FC and AC. An inherent assumption here is that ICMS-evoked activation [i.e., effective connectivity (EC)] accurately reports AC (Ferezou et al., 2007; Matsui et al., 2011; Grimaldi et al., 2016; Card and Gharbawie, 2020; Friedman et al., 2020b). Indeed, that assumption was confirmed in the fit that we reported between AC maps and EC maps. In using EC as a surrogate for AC, we increased the number of comparisons between FC and AC by ~10x (5 tracer sites vs 48 ICMS sites). High correspondence in those comparisons confirmed a tight relationship between FC and AC throughout the sensorimotor network. Similarly, the poor fit observed between FC and EC for non-matching sites points to the spatial specificity in both methods, which was likely conferred from monosynaptic connections.

Several features of our experimental design likely contributed to the detection of high correspondence between FC and AC. (1) FC and AC were compared at identical locations. (2) FC and AC were measured at columnar and cellular resolution, respectively. (3) Seed diameters were small and matched the size of tracer injection cores. (4) FC maps were thresholded to only retain pixels that reported connectivity across recordings. (5) Histological sectioning matched the planar view of the optical images, which facilitated accurate co-registration of FC and AC. (6) Our testbed was motor and somatosensory cortical areas, which form relatively strong network(s). (7) We compared FC to AC in the ipsilateral hemisphere only. Although discrepancies between FC and AC have been reported within hemisphere (Howells et al., 2020), they are more widely reported for interhemispheric connectivity (Greicius et al., 2009; Matsui et al., 2011; Adachi et al., 2012; Bauer et al., 2018; Thomas et al., 2021; c.f. Shen et al., 2015). For example, FC linking homotopic cortex has been reported for foci that lack interhemispheric connections (Vincent et al., 2007) and even in cases of corpus callosum agenesis (Tyszka et al., 2011). Thus, had we examined the opposite hemisphere in our preparation, then we may have found less fidelity between FC and AC and between FC and EC as compared to our observations in the ipsilateral hemisphere.

4.5. Previous comparisons of FC and AC

Previous efforts to understand the relationship between FC and AC have spanned various methods and species. For example, many human studies have compared FC patterns from RS-fMRI to fiber tract patterns from diffusion weighted imaging (dMRI) (Hagmann et al., 2008; Greicius et al., 2009; Heuvel et al., 2009; Honey et al., 2009; Adachi et al., 2012).

Within subject comparisons are a major strength in those studies, but the acquisition tools themselves lack the effective resolution for fine network architecture. In fMRI for example, signal-to-noise ratio and voxel size (≥1 mm isotropic) can blend nearby patches. Similarly, in vivo protocols of dMRI are limited in their sensitivity to detecting large, myelinated, fibers and have yet to match the level of detail achieved in *ex vivo* scans (Liu et al., 2020). In contrast, tracer injections, like in the present study, reveal site connections at cellular resolution. Several studies in monkeys have shown strong correspondence between FC from RS-fMRI and AC from tracer injections (Shen et al., 2012; Wang et al., 2013; Hori et al., 2020a). Those comparisons offer considerably higher spatial resolution than is feasible in the human studies, but they are still limited by the effective resolution of fMRI and the potential blurring that occurs from co-registering FC and AC from separate animals. Some rodent studies have compared FC from optical imaging to AC from tracer injections (Mohajerani et al., 2013; Bauer et al., 2018). Such comparisons ensure that FC and AC were both acquired at high spatial resolution, but the effective resolution in those comparisons is still limited by the impact of co-registering FC and AC from separate animals. Our experimental design remedied most of the issues discussed here, but of course our approach is not without its own limitations. For example, ISOI cannot measure activity in subcortical structures or cortical sulci. Also, deploying three connectivity methods in the same hemisphere limits the number of sites that can be practically investigated with ICMS or with tracers. In contrast, retrieving anatomical connectivity form curated repositories (e.g., CoCoMac, Marmoset Brain Connectivity Atlas, and Allen Brain Atlas) removes those constraints. Finally, the cranial window needed for ISOI limits its use in humans to subpopulations undergoing cranial surgery.

4.6. EEG indicates animal state and FC quality

Correspondence was highest between FC and AC during *light sedation*. FC quality deteriorated in *semi-deep sedation* (EEG burst-suppression) and deteriorated further in *deep sedation* (EEG suppression). The relationship between FC quality and animal state was consistent with previous reports (Liu et al., 2013b; Hutchison et al., 2014; Areshenkoff et al., 2021). Also, the *light* state was maintained here with isoflurane dose 0.5–1.5%, which is consistent with concentrations previously recommended for high quality maps in monkey RS-fMRI (Hutchison et al., 2014). Nevertheless, we also accrued extensive observations in the same monkeys where the same isoflurane dose induced periodic EEG suppression, or even complete EEG suppression. We concluded from those observations that a pre-set isoflurane concentration does not guarantee that the desired *light* state will be maintained, or even achieved. Our mitigation strategy was to confirm from EEG patterns that an animal was in the *light* state for several minutes before resting sate recording commenced. Our results confirmed that intracranial EEG patterns are reliable indicators of animal state and by extension FC quality.

5. Conclusion

We showed that FC maps from RS-ISOI report cortical connectivity with remarkable fidelity and in granular detail. RS-ISOI combines strengths from fMRI and optical methods that make it an attractive solution for mapping cortical architecture. RS-ISOI has the potential to serve many questions in systems neuroscience particularly where RS-fMRI is not feasible or high-resolution FC maps are desired.

Supplementary Material

Refer to Web version on PubMed Central for supplementary material.

Acknowledgments

Project was supported with funds from NIH (R01 NS105697) and University of Pittsburgh Brain Institute. We are grateful to ToniAnn Zullo for outstanding animal care before, after, and during, all procedures. We thank Drs. Alberto L. Vazquez, Aaron P. Batista, and Peter L. Strick, for many insightful discussions about the project. We thank Dr. David Schaeffer for critical feedback on an earlier version of the manuscript.

References

Adachi Y, Osada T, Sporns O, Watanabe T, Matsui T, Miyamoto K, Miyashita Y, 2012. Functional connectivity between anatomically unconnected areas is shaped by collective network-level effects in the macaque cortex. Cereb. Cortex 22, 1586–1592. [PubMed: 21893683]

Areshenkoff CN, Nashed JY, Hutchison RM, Hutchison M, Levy R, Cook DJ, Menon RS, Everling S, Gallivan JP, 2021. Muting, not fragmentation, of functional brain networks under general anesthesia. Neuroimage 231, 117830. [PubMed: 33549746]

Arieli A, Shoham D, Hildesheim R, Grinvald A, 1995. Coherent spatiotemporal patterns of ongoing activity revealed by real-time optical imaging coupled with single-unit recording in the cat visual cortex. J. Neurophysiol 73, 2072–2093. [PubMed: 7623099]

Baldwin MKL, Cooke DF, Krubitzer L, 2016. Intracortical microstimulation maps of motor, somatosensory, and posterior parietal cortex in tree shrews (Tupaia belangeri) reveal complex movement representations. Cereb. Cortex.

Bauer AQ, Kraft AW, Baxter GA, Wright PW, Reisman MD, Bice AR, Park JJ, Bruchas MR, Snyder AZ, Lee J, Culver JP, 2018. Effective connectivity measured using optogenetically evoked hemodynamic signals exhibits topography distinct from resting state functional connectivity in the mouse. Cereb. Cortex 28, 370–386. [PubMed: 29136125]

Birn RM, Molloy EK, Patriat R, Parker T, Meier TB, Kirk GR, Nair VA, Meyerand ME, Prabhakaran V, 2013. The effect of scan length on the reliability of resting-state fMRI connectivity estimates. Neuroimage 83, 550–558. [PubMed: 23747458]

Biswal B, Yetkin FZ, Haughton VM, Hyde JS, 1995. Functional connectivity in the motor cortex of resting human brain using echo-planar MRI. Magn. Reson. Med 34, 537–541. [PubMed: 8524021]

Bonhoeffer T, Grinvald A, 1991. Iso-orientation domains in cat visual cortex are arranged in pinwheel-like patterns. Nature 353, 429–431. [PubMed: 1896085]

Bruce K, Grofova I, 1992. Notes on a light and electron microscopic double-labeling method combining anterograde tracing with Phaseolus vulgaris leucoagglutinin and retrograde tracing with cholera toxin subunit B. J. Neurosci. Methods 45, 23–33. [PubMed: 1283431]

Buckner RL, Krienen FM, Yeo BTT, 2013. Opportunities and limitations of intrinsic functional connectivity MRI. Nat. Neurosci 16, 832–837. [PubMed: 23799476]

Bullmore E, Sporns O, 2009. Complex brain networks: graph theoretical analysis of structural and functional systems. Nat. Rev. Neurosci 10, 186–198. [PubMed: 19190637]

Card NS, Gharbawie OA, 2020. Principles of intrinsic motor cortex connectivity in primates. J. Neurosci 40, 4348–4362. [PubMed: 32327531]

Chan AW, Mohajerani MH, LeDue JM, Wang YT, Murphy TH, 2015. Mesoscale infraslow spontaneous membrane potential fluctuations recapitulate high-frequency activity cortical motifs. Nat. Commun 6, 7738. [PubMed: 26190168]

Chen G, Wang F, Gore JC, Roe AW, 2013. Layer-specific BOLD activation in awake monkey V1 revealed by ultra-high spatial resolution functional magnetic resonance imaging. Neuroimage 64, 147–155. [PubMed: 22960152]

Cordes D, Haughton VM, Arfanakis K, Carew JD, Turski PA, Moritz CH, Quigley MA, Meyerand ME, 2001. Frequencies contributing to functional connectivity in the cerebral cortex in “resting-state” data. AJNR Am. J. Neuroradiol 22, 1326–1333. [PubMed: 11498421]

Dancause N, Barbay S, Frost SB, Plautz EJ, Popescu M, Dixon PM, Stowe AM, Friel KM, Nudo RJ, 2006a. Topographically divergent and convergent connectivity between premotor and primary motor cortex. Cereb. Cortex 16, 1057–1068. [PubMed: 16221929]

Dancause N, Barbay S, Frost SB, Plautz EJ, Stowe AM, Friel KM, Nudo RJ, 2006b. Ipsilateral connections of the ventral premotor cortex in a new world primate. J. Comp. Neurol 495, 374–390. [PubMed: 16485282]

Dancause N, Duric V, Barbay S, Frost SB, Stylianou A, Nudo RJ, 2008. An additional motor-related field in the lateral frontal cortex of squirrel monkeys. Cereb. Cortex 18, 2719–2728. [PubMed: 18424778]

Devor A, Dunn AK, Andermann ML, Ulbert I, Boas DA, Dale AM, 2003. Coupling of total hemoglobin concentration, oxygenation, and neural activity in rat somatosensory cortex. Neuron 39, 353–359. [PubMed: 12873390]

Dum RP, Strick PL, 2005. Frontal lobe inputs to the digit representations of the motor areas on the lateral surface of the hemisphere. J. Neurosci 25, 1375–1386. [PubMed: 15703391]

Ekstrom LB, Roelfsema PR, Arsenault JT, Bonmassar G, Vanduffel W, 2008. Bottom-up dependent gating of frontal signals in early visual cortex. Science 321, 414–417. [PubMed: 18635806]

Ferezou I, Haiss F, Gentet LJ, Aronoff R, Weber B, Petersen CCH, 2007. Spatiotemporal dynamics of cortical sensorimotor integration in behaving mice. Neuron 56, 907–923. [PubMed: 18054865]

Fox MD, Raichle ME, 2007. Spontaneous fluctuations in brain activity observed with functional magnetic resonance imaging. Nat. Rev. Neurosci 8, 700–711. [PubMed: 17704812]

Friedman RM, Morone KA, Gharbawie OA, Roe AW, 2020a. Mapping mesoscale cortical connectivity in monkey sensorimotor cortex with optical imaging and microstimulation. J. Comp. Neurol 1.

Friedman RM, Morone KA, Gharbawie OA, Roe AW, 2020b. Mapping mesoscale cortical connectivity in monkey sensorimotor cortex with optical imaging and microstimulation. J. Comp. Neurol.

Gharbawie OA, Stepniewska I, Kaas JH, 2011a. Cortical connections of functional zones in posterior parietal cortex and frontal cortex motor regions in new world monkeys. Cereb. Cortex.

Gharbawie OA, Stepniewska I, Qi H, Kaas JH, 2011b. Multiple parietal-frontal pathways mediate grasping in macaque monkeys. J. Neurosci 31, 11660–11677. [PubMed: 21832196]

Gould HJ, Cusick CG, Pons TP, Kaas JH, 1986. The relationship of corpus callosum connections to electrical stimulation maps of motor, supplementary motor, and the frontal eye fields in owl monkeys. J. Comp. Neurol 247, 297–325. [PubMed: 3722441]

Graziano MSA, Taylor CSR, Moore T, 2002. Complex movements evoked by microstimulation of precentral cortex. Neuron 34, 841–851. [PubMed: 12062029]

Greicius MD, Supekar K, Menon V, Dougherty RF, 2009. Resting-state functional connectivity reflects structural connectivity in the default mode network. Cereb. Cortex 19, 72–78. [PubMed: 18403396]

Grimaldi P, Saleem KS, Tsao D, 2016. Anatomical connections of the functionally defined “face patches” in the macaque monkey. Neuron 90, 1325–1342. [PubMed: 27263973]

Grinvald A, Slovin H, Vanzetta I, 2000. Non-invasive visualization of cortical columns by fMRI. Nat. Neurosci 3, 105–107. [PubMed: 10649563]

Hagmann P, Cammoun L, Gigandet X, Meuli R, Honey CJ, Wedeen VJ, Sporns O, 2008. Mapping the structural core of human cerebral cortex. PLoS Biol 6, e159. [PubMed: 18597554]

Hamadjida A, Dea M, Deffeyes J, Quessy S, Dancause N, 2016. Parallel cortical networks formed by modular organization of primary motor cortex outputs. Curr. Biol 26, 1737–1743. [PubMed: 27322001]

Heuvel MP, van den, Mandl RCW, Kahn RS, Pol HEH, 2009. Functionally linked resting-state networks reflect the underlying structural connectivity architecture of the human brain. Hum. Brain Mapp 30, 3127–3141. [PubMed: 19235882]

Honey CJ, Sporns O, Cammoun L, Gigandet X, Thiran JP, Meuli R, Hagmann P, 2009. Predicting human resting-state functional connectivity from structural connectivity. Proc. Natl. Acad. Sci. USA 106, 2035–2040. [PubMed: 19188601]

Hori Y, Schaeffer DJ, Gilbert KM, Hayrynen LK, Cléry JC, Gati JS, Menon RS, Everling S, 2020a. Comparison of resting-state functional connectivity in marmosets with tracer-based cellular connectivity. Neuroimage 204, 116241. [PubMed: 31586676]

Hori Y, Schaeffer DJ, Gilbert KM, Hayrynen LK, Cléry JC, Gati JS, Menon RS, Everling S, 2020b. Altered resting-state functional connectivity between awake and isoflurane anesthetized marmosets. Cereb. Cortex 1–17. [PubMed: 31220218]

Howells H, Simone Luciano, Borra E, Luca Fornia·, Cerri G, Luppino G, 2020. Reproducing macaque lateral grasping and oculomotor networks using resting state functional connectivity and diffusion tractography. Brain Struct. Funct 225, 2533–2551. [PubMed: 32936342]

Huber L, Handwerker DA, Jangraw DC, Chen G, Hall A, Stüber C, Gonzalez-Castillo J, Ivanov D, Marrett S, Guidi M, Goense J, Poser BA, Bandettini PA, 2017. High-resolution CBV-fMRI allows mapping of laminar activity and connectivity of cortical input and output in human M1. Neuron 96, 1253–1263 e7. [PubMed: 29224727]

Hutchison RM, Everling S, 2012. Monkey in the middle: why non-human primates are needed to bridge the gap in resting-state investigations. Front. Neuroanat 6, 29. [PubMed: 22855672]

Hutchison RM, Hutchison M, Manning KY, Menon RS, Everling S, 2014. Isoflurane induces dose-dependent alterations in the cortical connectivity profiles and dynamic properties of the brain's functional architecture. Hum. Brain Mapp 35, 5754–5775. [PubMed: 25044934]

Kim DS, Duong TQ, Kim SG, 2000. High-resolution mapping of iso-orientation columns by fMRI. Nat. Neurosci 3, 164–169. [PubMed: 10649572]

Klink PC, et al. , 2021. Combining brain perturbation and neuroimaging in non-human primates. Neuroimage 235, 118017. [PubMed: 33794355]

Kura S, Xie H, Fu B, Ayata C, Boas DA, Sakadžić S, 2018. Intrinsic optical signal imaging of the blood volume changes is sufficient for mapping the resting state functional connectivity in the rodent cortex. J. Neural Eng 15, 035003. [PubMed: 29451130]

Liao C-C, Gharbawie OA, Qi H, Kaas JH, 2013. Cortical connections to single digit representations in area 3b of somatosensory cortex in squirrel monkeys and prosimian galagos. J. Comp. Neurol 521, 3768–3790. [PubMed: 23749740]

Liu JV, Hirano Y, Nascimento GC, Stefanovic B, Leopold DA, Silva AC, 2013a. fMRI in the awake marmoset: somatosensory-evoked responses, functional connectivity, and comparison with propofol anesthesia. Neuroimage 78, 186–195. [PubMed: 23571417]

Liu X, Pillay S, Li R, Vizuete JA, Pechman KR, Schmainda KM, Hudetz AG, 2013b. Multiphasic modification of intrinsic functional connectivity of the rat brain during increasing levels of propofol. Neuroimage 83, 581–592. [PubMed: 23851326]

Liu X, Zhu X-H, Zhang Y, Chen W, 2013c. The change of functional connectivity specificity in rats under various anesthesia levels and its neural origin. Brain Topogr 26, 363–377. [PubMed: 23208517]

Liu C, Ye FQ, Newman JD, Szczupak D, Tian X, Yen CC-C, Majka P, Glen D, Rosa MGP, Leopold DA, Silva AC, 2020. A resource for the detailed 3D mapping of white matter pathways in the marmoset brain. Nat. Neurosci 23, 271–280. [PubMed: 31932765]

Logothetis NK, Pauls J, Augath M, Trinath T, Oeltermann A, 2001. Neurophysiological investigation of the basis of the fMRI signal. Nature 412, 150–157. [PubMed: 11449264]

Lu HD, Roe AW, 2007. Optical imaging of contrast response in Macaque monkey V1 and V2. Cereb. Cortex 17, 2675–2695. [PubMed: 17264252]

Matsui T, Tamura K, Koyano KW, Takeuchi D, Adachi Y, Osada T, Miyashita Y, 2011. Direct comparison of spontaneous functional connectivity and effective connectivity measured by intracortical microstimulation: an fMRI study in macaque monkeys. Cereb. Cortex 21, 2348–2356. [PubMed: 21368090]

Mayer A, Baldwin MKL, Cooke DF, Lima BR, Padberg J, Lewenfus G, Franca JG, Krubitzer L, 2019. The multiple representations of complex digit movements in primary motor cortex form the building blocks for complex grip types in capuchin monkeys. J. Neurosci 39, 6684–6695. [PubMed: 31235643]

Mayhew JEW, Askew S, Zheng Y, Porrill J, Westby GWM, Redgrave P, Rector DM, Harper RM, 1996. Cerebral vasomotion: a 0.1-Hz oscillation in reflected light imaging of neural activity. Neuroimage 4, 183–193. [PubMed: 9345508]

Ma Y, Shaik MA, Kozberg MG, Kim SH, Portes JP, Timerman D, Hillman EMC, 2016. Resting-state hemodynamics are spatiotemporally coupled to synchronized and symmetric neural activity in excitatory neurons. Proc. Natl. Acad. Sci. USA 113, E8463–E8471. [PubMed: 27974609]

Merzenich MM, Kaas JH, Sur M, Lin CS, 1978. Double representation of the body surface within cytoarchitectonic areas 3b and 1 in “SI” in the owl monkey (Aotus trivirgatus). J. Comp. Neurol 181, 41–73. [PubMed: 98537]

Moeller S, Freiwald WA, Tsao DY, 2008. Patches with links: a unified system for processing faces in the macaque temporal lobe. Science 320, 1355–1359. [PubMed: 18535247]

Mohajerani MH, Chan AW, Mohsenvand M, LeDue J, Liu R, McVea DA, Boyd JD, Wang YT, Reimers M, Murphy TH, 2013. Spontaneous cortical activity alternates between motifs defined by regional axonal projections. Nat. Neurosci 16, 1426–1435. [PubMed: 23974708]

Mohajerani MH, McVea DA, Fingas M, Murphy TH, 2010. Mirrored bilateral slow-wave cortical activity within local circuits revealed by fast bihemispheric voltage-sensitive dye imaging in anesthetized and awake mice. J. Neurosci 30, 3745–3751. [PubMed: 20220008]

Murphy K, Fox MD, 2017. Towards a consensus regarding global signal regression for resting state functional connectivity MRI. Neuroimage 154, 169–173. [PubMed: 27888059]

Négyessy L, Pálfi E, Ashaber M, Palmer C, Jákli B, Friedman RM, Chen LM, Roe AW, 2013. Intrinsic horizontal connections process global tactile features in the primary somatosensory cortex: neuroanatomical evidence. J. Comp. Neurol 521, 2798–2817. [PubMed: 23436325]

Padberg J, Disbrow E, Krubitzer L, 2005. The organization and connections of anterior and posterior parietal cortex in titi monkeys: do new world monkeys have an area 2? Cereb. Cortex 15, 1938–1963. [PubMed: 15758196]

Sakas DE, Charnvises K, Borges LF, Zervas NT, 1990. Biologically inert synthetic dural substitutes. Appraisal of a medical-grade aliphatic polyurethane and a polysiloxane-carbonate block copolymer. J. Neurosurg 73, 936–941. [PubMed: 2230977]

Schilling KG, Gao Y, Christian M, Janve V, Stepniewska I, Landman BA, Anderson AW, 2019. A web-based atlas combining MRI and histology of the squirrel monkey brain. Neuroinformatics 17, 131–145. [PubMed: 30006920]

Schölvinck ML, Maier A, Ye FQ, Duyn JH, Leopold DA, 2010. Neural basis of global resting-state fMRI activity. Proc. Natl. Acad. Sci. USA 107, 10238–10243. [PubMed: 20439733]

Shen K, Bezgin G, Hutchison RM, Gati JS, Menon RS, Everling S, McIntosh AR, 2012. Information processing architecture of functionally defined clusters in the macaque cortex. J. Neurosci 32, 17465–17476. [PubMed: 23197737]

Shen K, Mišić B, Cipollini BN, Bezgin G, Buschkuehl M, Hutchison RM, Jaeggi SM, Kross E, Peltier SJ, Everling S, Jonides J, McIntosh AR, Berman MG, 2015. Stable long-range interhemispheric coordination is supported by direct anatomical projections. Proc. Natl. Acad. Sci. USA 112, 6473–6478. [PubMed: 25941372]

Sheth SA, Nemoto M, Guiou M, Walker M, Pouratian N, Hageman N, Toga AW, 2004. Columnar specificity of microvascular oxygenation and volume responses: implications for functional brain mapping. J. Neurosci 24, 634–641. [PubMed: 14736849]

Shi Z, Wu R, Yang P-F, Wang F, Wu T-L, Mishra A, Chen LM, Gore JC, 2017. High spatial correspondence at a columnar level between activation and resting state fMRI signals and local field potentials. Proc. Natl. Acad. Sci. USA 114, 5253–5258. [PubMed: 28461461]

Shmuel A, Leopold DA, 2008. Neuronal correlates of spontaneous fluctuations in fMRI signals in monkey visual cortex: implications for functional connectivity at rest. Hum. Brain Mapp 29, 751–761. [PubMed: 18465799]

Stepniewska I, Fang P-C, Kaas JH, 2005. Microstimulation reveals specialized subregions for different complex movements in posterior parietal cortex of prosimian galagos. Proc. Natl. Acad. Sci. USA 102, 4878–4883. [PubMed: 15772167]

Stepniewska I, Friedman RM, Gharbawie OA, Cerkevich CM, Roe AW, Kaas JH, 2011. Optical imaging in galagos reveals parietal-frontal circuits underlying motor behavior. Proc. Natl. Acad. Sci. USA 108, E725–E732. [PubMed: 21873212]

Stepniewska I, Preuss TM, Kaas JH, 1993. Architectonics, somatotopic organization, and ipsilateral cortical connections of the primary motor area (M1) of owl monkeys. J. Comp. Neurol 330, 238–271. [PubMed: 7684050]

Stepniewska I, Preuss TM, Kaas JH, 2006. Ipsilateral cortical connections of dorsal and ventral premotor areas in New World owl monkeys. J. Comp. Neurol 495, 691–708. [PubMed: 16506197]

Sur M, Nelson RJ, Kaas JH, 1982. Representations of the body surface in cortical areas 3b and 1 of squirrel monkeys: comparisons with other primates. J. Comp. Neurol 211, 177–192. [PubMed: 7174889]

Thomas J, Sharma D, Mohanta S, Jain N, 2021. Resting-State functional networks of different topographic representations in the somatosensory cortex of macaque monkeys and humans. Neuroimage 228, 117694. [PubMed: 33385552]

Tolias AS, Sultan F, Augath M, Oeltermann A, Tehovnik EJ, Schiller PH, Logothetis NK, 2005. Mapping cortical activity elicited with electrical microstimulation using fMRI in the macaque. Neuron 48, 901–911. [PubMed: 16364895]

Tyszka JM, Kennedy DP, Adolphs R, Paul LK, 2011. Intact bilateral resting-state networks in the absence of the corpus callosum. J. Neurosci 31, 15154–15162. [PubMed: 22016549]

Vanni MP, Chan AW, Balbi M, Silasi G, Murphy TH, 2017. Mesoscale mapping of mouse cortex reveals frequency-dependent cycling between distinct macroscale functional modules. J. Neurosci 37, 7513–7533. [PubMed: 28674167]

Vasireddi AK, Vazquez AL, Whitney DE, Fukuda M, Kim S-G, 2016. Functional connectivity of resting hemodynamic signals in submillimeter orientation columns of the visual cortex. Brain Connect 6, 596–606. [PubMed: 27461173]

Vazquez AL, Murphy MC, Kim S-G, 2014. Neuronal and physiological correlation to hemodynamic resting-state fluctuations in health and disease. Brain Connect 4, 727–740. [PubMed: 25300278]

Vincent JL, Patel GH, Fox MD, Snyder AZ, Baker JT, Van Essen DC, Zempel JM, Snyder LH, Corbetta M, Raichle ME, 2007. Intrinsic functional architecture in the anaesthetized monkey brain. Nature 447, 83–86. [PubMed: 17476267]

Wang Z, Chen LM, Négyessy L, Friedman RM, Mishra A, Gore JC, Roe AW, 2013. The relationship of anatomical and functional connectivity to resting-state connectivity in primate somatosensory cortex. Neuron 78, 1116–1126. [PubMed: 23791200]

Welker WI, Benjamin RM, Miles RC, Woolsey CN, 1957. Motor effects of stimulation of cerebral cortex of squirrel monkey (Saimiri sciureus). J. Neurophysiol 20, 347–364. [PubMed: 13439407]

White BR, Bauer AQ, Snyder AZ, Schlaggar BL, Lee J-M, Culver JP, 2011. Imaging of functional connectivity in the mouse brain. PLoS One 6, e16322. [PubMed: 21283729]

Yeo BTT, Krienen FM, Sepulcre J, Sabuncu MR, Lashkari D, Hollinshead M, Roffman JL, Smoller JW, Zöllei L, Polimeni JR, Fischl B, Liu H, Buckner RL, 2011. The organization of the human cerebral cortex estimated by intrinsic functional connectivity. J. Neurophysiol 106, 1125–1165. [PubMed: 21653723]

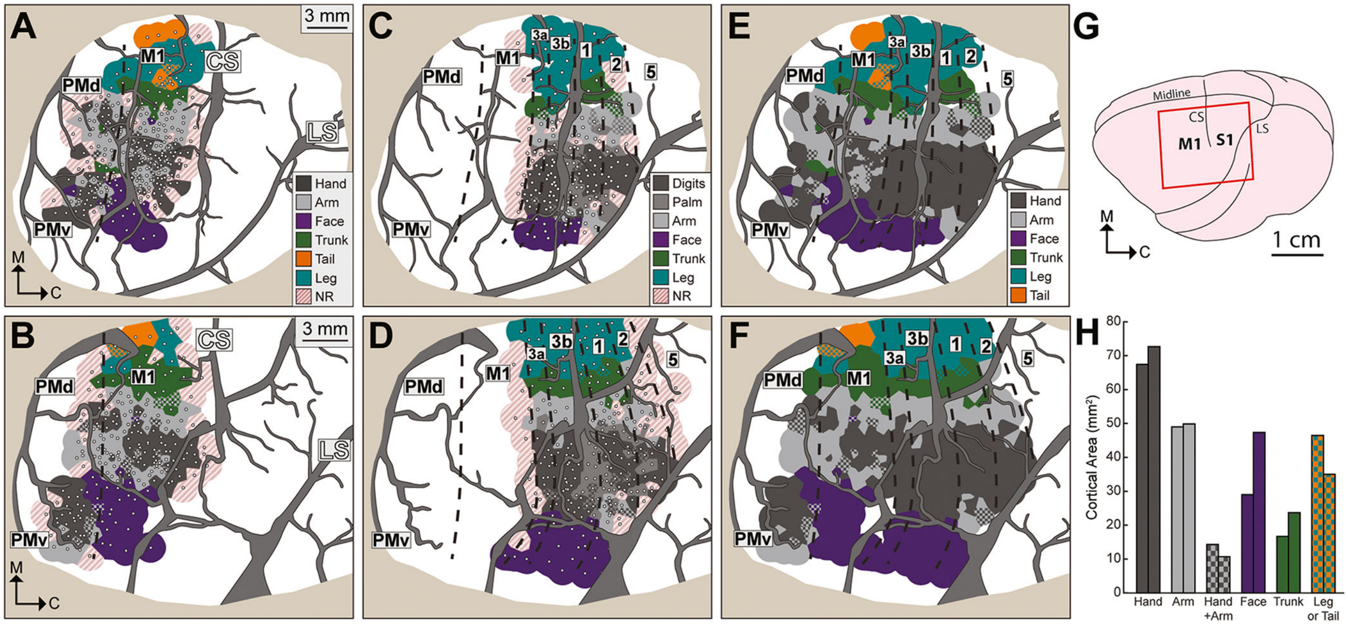

Fig. 1.

Motor and somatosensory maps are consistent between animals. (A) Motor maps for M1, PMd, and PMv from the left hemisphere (monkey B). White dots are intracortical microstimulation sites (ICMS, n = 264). Voronoi tiles (1.0 mm radius) are color-coded according to ICMS-evoked movement. Checkered tiles depict multiple movements (1 color/ body part). Non-responsive sites (NR) failed to evoke movements at 150 μA. The forelimb representation (gray tones) was mapped up to its borders. Face, leg, and tail representations were mapped less extensively. The rostral M1 border (dashed line) was estimated from current thresholds and distance to central sulcus (CS). Major vessels are masked in gray. LS: lateral sulcus. Tan color in the perimeter masks resected dura and skull. Scale bar applies to panels in top row. (B) Motor map (n = 231 sites) from monkey R. Scale bar applies to panels in bottom row. (C) Somatosensory maps for areas 3a, 3b, 1, and 2, from the same hemisphere in (A). White dots are microelectrode recording sites (n = 169). Voronoi tiles (1.0 mm radius) are color-coded according to body part that drove unit activity most effectively. Sites were classified as NR if stimulation and joint manipulation failed to drive unit activity. Cortical borders (dashed lines) were estimated from receptive fields and distance to CS. (D) Somatosensory maps (n = 251 sites) from the same hemisphere in (B). (E) Combined maps from (A) and (C). NR sites were removed. Somatosensory sites with palm and digit responses are classified here as hand. (F) Combined maps from (B) and (D). (G) Schematic of squirrel monkey brain. Red rectangle approximates the field of view in (A-F). (H) Cortical surface areas measured from (E) and (F).

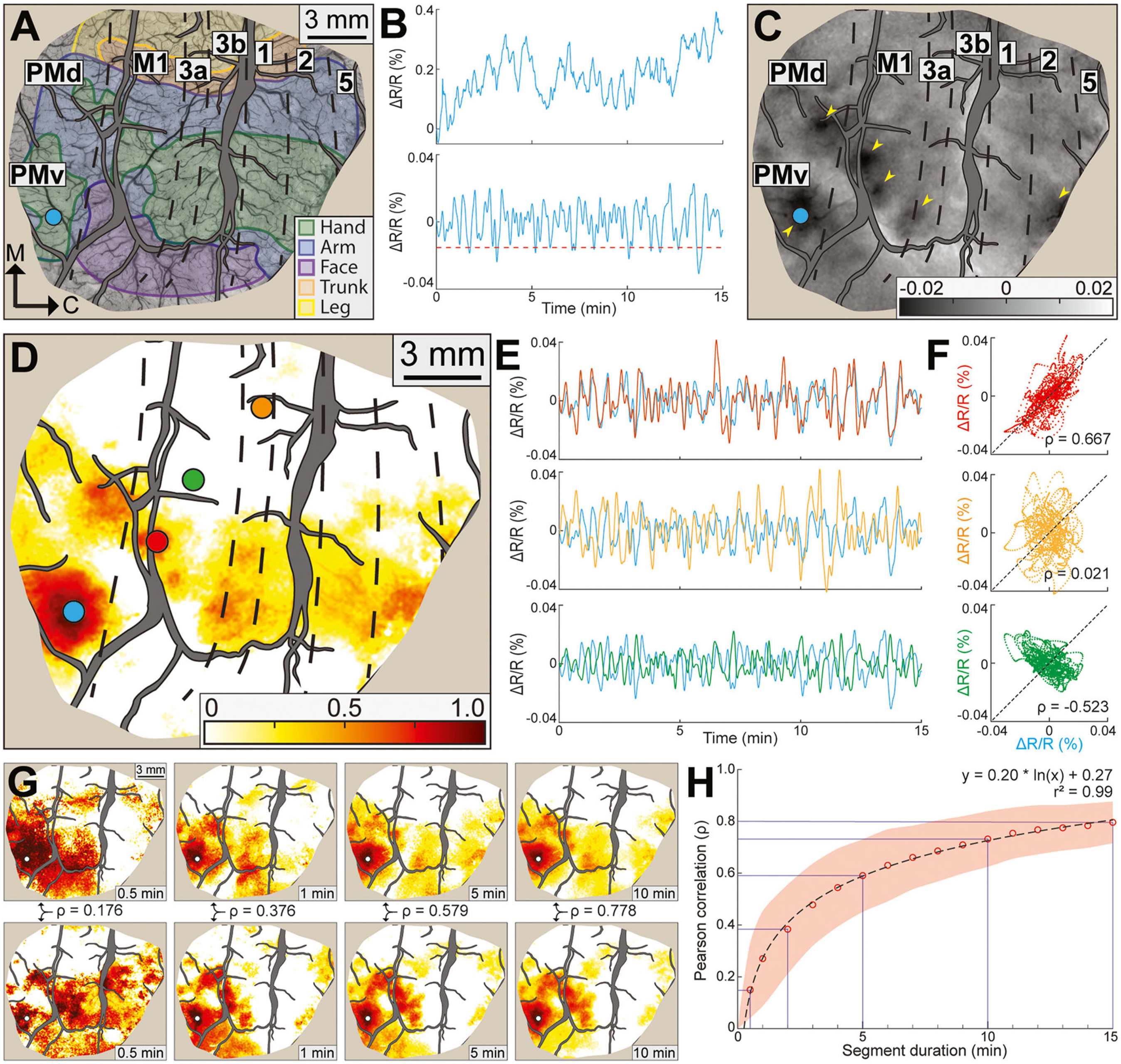

Fig. 2.

Time course correlations and optimal imaging duration. (A) Optical image of cortex (528 nm illumination) with cortical borders and zones from microelectrode maps. Large blood vessels are masked in gray. Tan color around the perimeter masks resected dura and skull. Scale bar is same for (C). Seed (blue circle) is in the PMv hand zone. (B) *Top*. Raw time course of reflectance change (ΔR/R%) measured from the seed in 1 RS-ISOI recording. *Bottom*. Same time course after spatial and temporal processing. Dashed line is threshold for flagging frames where the seed darkened. (C) Average optical image from frames flagged in (B). Dark patches (arrowheads) are evident at the seed and in PMd, M1, 3a, and area 2. (D) Functional connectivity (FC) map from same seed in (C). Color scale reflects the correlation coefficient (ρ) between the time course at a given pixel and the time course of the seed. Colored circles are representative regions-of-interest (ROIs). (E) Each plot shows time courses from the seed and 1 ROI from (D). Line color matches ROI color in (D). (F) Scatter plots show reflectance change in the seed (x-axis) against reflectance change in the ROIs (y-axis). Each plot relates to the adjacent line plot in (E). Only the red scatter plot showed positive correlation. (G) Representative FC maps generated from variable segments of a 30-min RS-ISOI recording. Segment duration is in the bottom right corner. Seed (white dot) is in the same location as (D). Coefficients (ρ) are from pairwise comparisons (Pearson correlation) between map in the top row and map directly below it. (H) Pairwise comparisons (n = 250,245 between both monkeys) of maps and coefficients from 4 RS-ISOI recordings. Red circles are average coefficients for each segment duration. Red shading is ± SD. Equation and r^2 describe line of best fit.

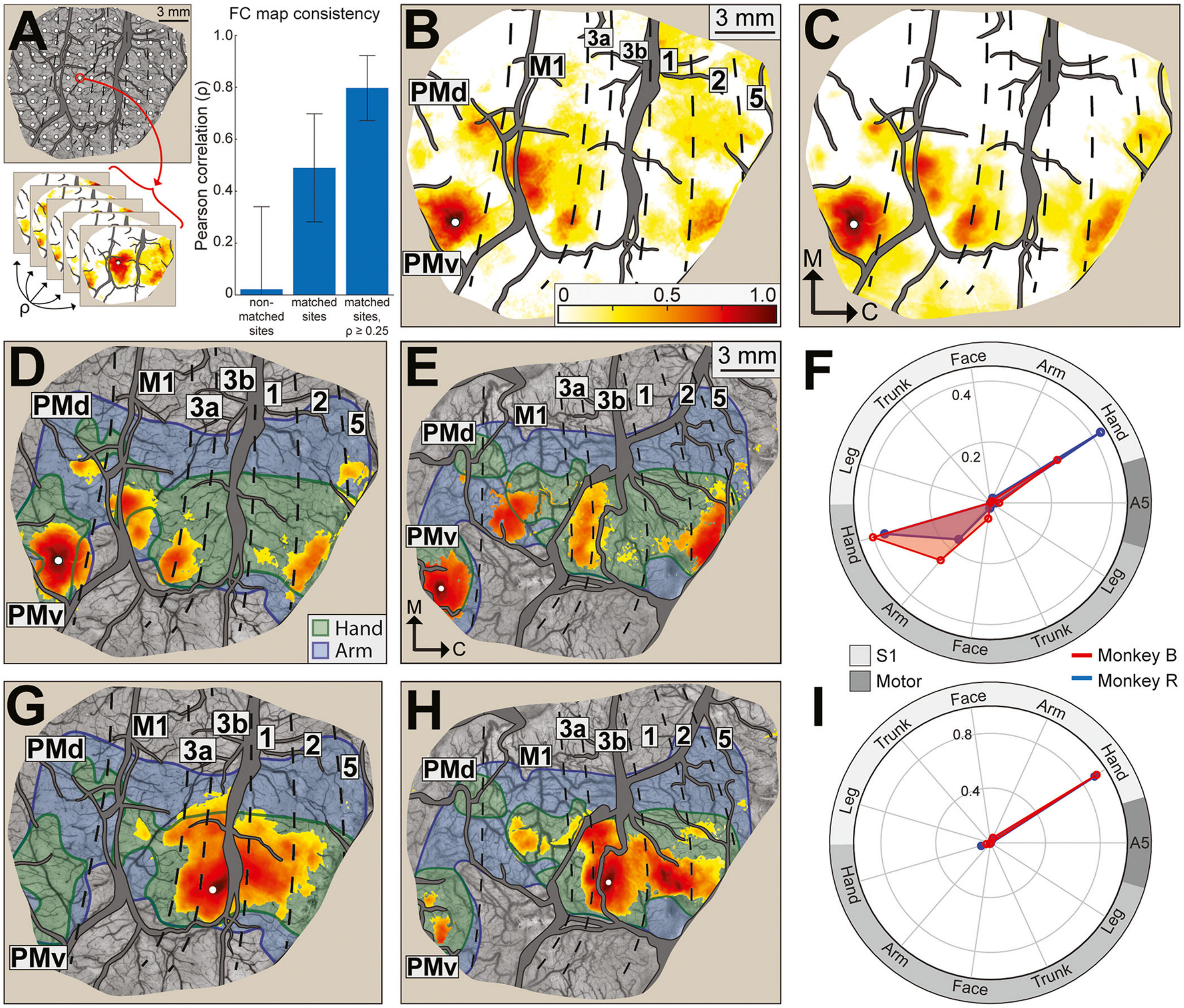

Fig. 3.

Functional connectivity maps are stable over months and consistent between monkeys. (A) Grid of seeds (n = 66–71 per hemisphere, 1 mm spacing). For every seed, FC maps were generated from imaging runs up to 16 months apart. *Bar plot.* Pairwise comparisons (Pearson correlation) of maps from each animal. Correspondence was highest for matched sites after maps were thresholded for coefficients ≥ 0.25. Correspondence declined in the absence of thresholding. There was no correspondence for comparisons between non-matched sites. (B) Functional connectivity (FC) map from a representative RS-ISOI recording (15 min) in monkey B. Seed (white dot) is in the PMv hand zone. Color bar is correlation coefficients (ρ) and applies to all panels. (C) Average FC map from 13 RS-ISOI recordings. Seed location is same as (B). Patches of hot colors are in similar locations in (B) and (C). (D) FC map is same as (C) but limited to pixels with significant coefficients (one-tailed t-test, $p < 0.001$). (E) Average FC map for a matching seed location in monkey R. Map is based on 15 RS-ISOI recordings. (F) FC profiled in relation to motor and somatosensory maps. Quantification is based on number of pixels and coefficients for maps in (D, red plot) and (E, blue plot). Sum of radial coordinates = 1. Functional zones are grouped according to modality. Motor includes M1, PMd, and PMv. S1 includes areas 3a, 3b, 1, and 2. Area 5 is independent (darkest gray). (G-I) Same as (D-F), but for a site in area 3b digit zone.

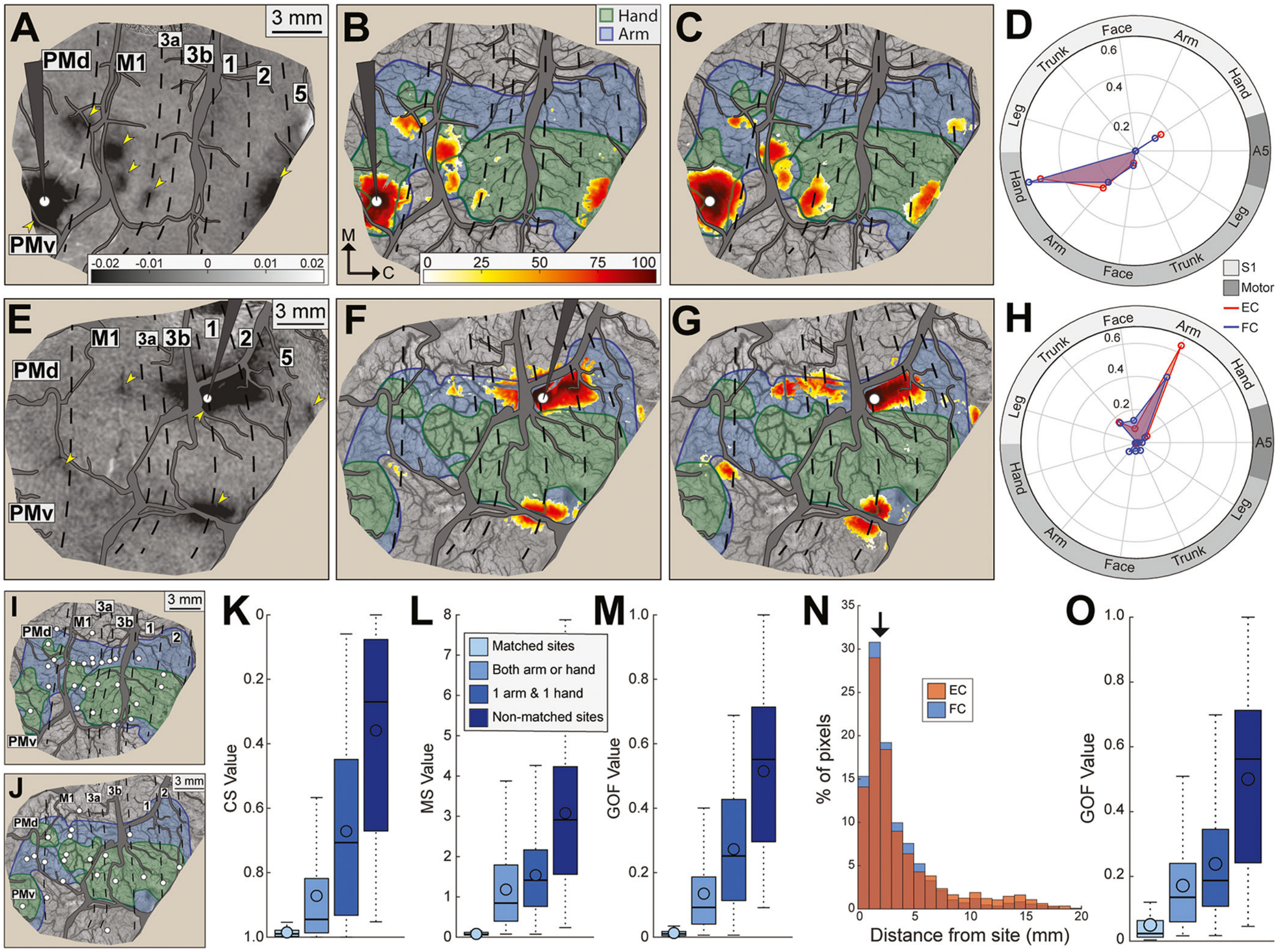

Fig. 4.

Functional connectivity maps correspond with effective connectivity maps. (A-D) Direct comparison of FC and EC maps from a site in the PMv hand zone (monkey B). (A) Average optical image: ICMS condition minus blank condition (50 trials/condition). Arrowheads point to dark patches evoked from ICMS. Stimulating microelectrode and major vessels are masked in gray. Microelectrode tip (white circle) was 1000 μm deep. (B) EC map: pixels that darkened (t-test, $p < 0.001$) in response to ICMS were ranked from lowest (white = 0th percentile) to highest (dark red = 100th percentile). (C) FC map for the same site in (A-B). Pixels with significant coefficients were percentile ranked as in (B). (D) Quantitative profile of FC (blue plot) and EC (red plot) maps in relation to motor and somatosensory maps. Near perfect overlap between maps was confirmed with cosine similarity (0.99). (E-H) Same as (A-D), but for a site in area 1 arm zone. Correspondence between maps was confirmed with cosine similarity (0.97). (I) Sites (n = 27) for direct comparison of FC and EC maps (monkey B). (J) Same as (I), but in monkey R (n = 21 sites). (K) Cosine similarity for pairwise comparisons between FC and EC maps. Comparisons were grouped according to site identity. (1) *Matched sites.* FC and EC maps were generated from identical locations. (2) *Both arm or hand.* FC and EC were generated from sites within the same forelimb zone (e.g., hand), but from different locations. (3) *1 arm & 1 hand*. FC and EC maps were generated from non-matched forelimb zones. (4) *Non-matched sites*. FC and EC maps were generated from non-matched representations of the body (e.g., 1 site in a forelimb zone and other site in face). (L) Mean separation between pixels for the same comparisons in (K). (M) Goodness of fit (GOF) for the same comparisons in (K). (N) Distribution of significant pixels in FC and EC maps as a function of distance from the 48 sites in (I-J). In FC and EC maps, ~50% of significant pixels were within 2 mm of the test site. (O) Same as (M) but after excluding significant pixels within 2 mm of each test site.

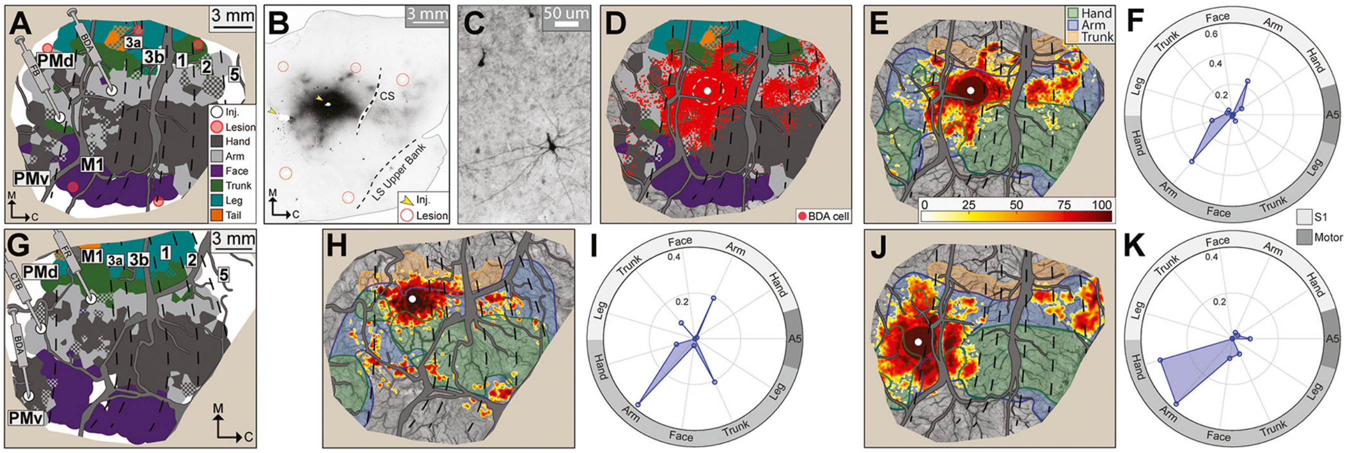

Fig. 5.

Anatomical connectivity maps from tracer injections. (A) Tracer injections (white dots) in M1 arm and PMd arm zones in monkey B. Red circles are microlesion sites. (B) Representative cortical section processed for BDA (horizontal plane, 50 μm thickness). Dark patches are labeled cells and axons. Section was cropped to the approximate field-of-view in (A). Arrowheads mark injection sites. CS: central sulcus; LS: lateral sulcus. (C) Representative BDA-labeled cell. (D) BDA-labeled cells (red circles, n = 12,136) collated from 8 horizontal sections. White dot marks BDA injection site. Dashed circle marks zone of dense tracer uptake that has been filled with red. (E) Anatomical connectivity (AC) map based on the BDA-labeled cells in (D). Cells were counted from circular bins (80 μm radius) that increased by 10 μm with every millimeter from the injection site. Bins with fewer than 2 cells were omitted for de-noising. Colors indicate rank percentile from lowest (white = 0th percentile) to highest (dark red = 100th percentile). Zone of dense tracer uptake is filled with the 90th percentile color. (F) Quantitative profile of (E) in relation to motor and somatosensory maps. (G) Tracer injections in M1 arm, PMd arm, and PMv hand in monkey R. (H) AC map from injection into the M1 arm zone in monkey R (6 sections, 2,832 FR-labeled cells). (I) Quantitative profile of (H). (J) AC map from injection into the PMd arm zone in monkey B (4 sections, 32,296 FB-labeled cells). (K) Quantitative profile of (J).

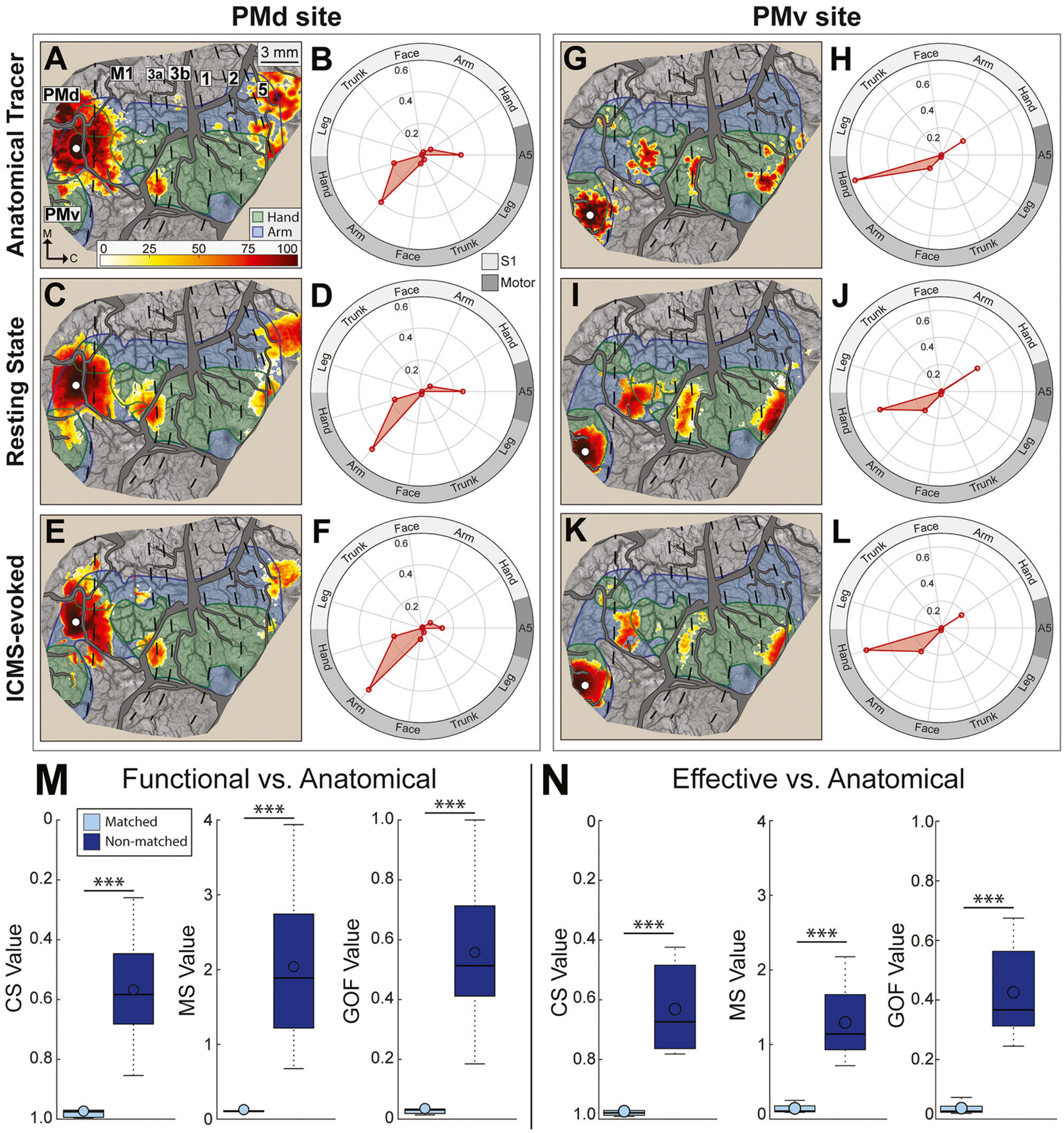

Fig. 6.

Functional and effective connectivity maps correspond with anatomical connectivity maps. (A-F) Comparison of FC, EC, and AC maps for a site in the PMd arm zone (monkey R). Conventions are consistent with Fig. 4 & Fig. 5. Color bar applies to all maps. Note similarities between the 3 maps and the 3 polar plots. (A-B) AC map and corresponding quantitative profile (5 sections, 50,020 CTB-labeled cells). (C-D) FC map and quantitative profile. (E-F) EC map and quantitative profile. (G-L) Same as (A-F), but for a site in the PMv hand zone. Note similarities between the 3 maps and the 3 polar plots. AC map in

(G) was based on 6 sections, 1,878 BDA-labeled cells. (M) Cosine similarity (CS), mean separation (MS), and goodness of fit (GOF) for pairwise comparisons of FC maps and AC maps from matched (light blue) and non-matched (dark blue) sites. Matched comparisons showed more correspondence between FC and AC maps than non-matched comparisons. (N) Matched comparisons showed more correspondence between EC and AC maps than non-matched comparisons.

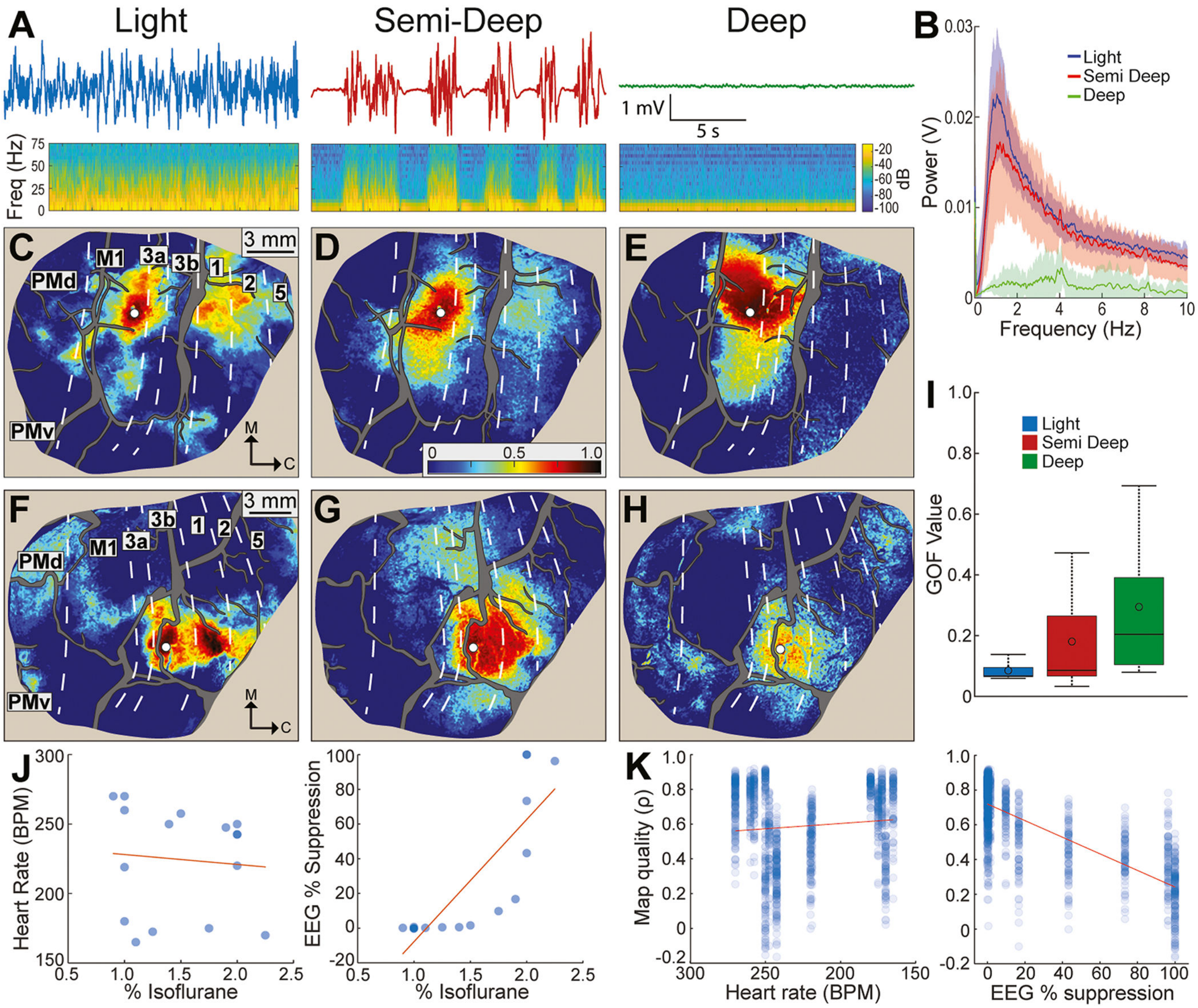

Fig. 7.

Relationship between animal state and FC map quality. (A) Representative EEG traces (top) and corresponding spectrograms (bottom) for 3 animal states. The *light* state consisted of slow waveforms and no suppression (0.9–1.5% isoflurane). The *semi-deep* state had periodic suppression (1.75–2.0% isoflurane). The *deep* state had suppression only (2.0–2.25% isoflurane). (B) Power spectrum (mean±SD) of EEG acquired during 16 RS-ISOI recordings (*light* n = 9, *semi-deep* n = 4, *deep* n = 3). (C-E) FC maps from one seed (white circle) in the M1 arm zone (monkey B). FC maps match the animal state directly above in (A). Note the deterioration in spatial patterns from *light* to *deep*. (F-H) Same as (C-E), but for a seed in area 3b digit zone (monkey R). (I) Goodness of fit (GOF) between FC and AC maps at the 5 tracer sites. GOF was lowest (best) in the *light* state. (J) Heart rate (left) and EEG suppression (right) as a function of isoflurane dose. Each point is an average from a 15-min recording. Red line is linear fit. (K) FC map quality as a function of heart rate (left) and EEG suppression (right). Map quality is the correlation coefficient (Pearson) from comparing individual FC maps with average FC maps from the same seeds. Comparisons were conducted in seeds throughout the field-of-view (n = 83–85 seeds per hemisphere).

Table 1

Procedures and data collected from each animal.

Monkey	Procedures	Motor Map Sites	Receptive Field Sites	Resting State Recordings	Effective Connectivity Sites	Tracer Injections
B	14	264	169	13	27	2
R	13	231	251	15	21	3
Total	27	465	420	28	48	5

Numbers are limited to data included in the present study.

Table 2

Animal state monitoring.

Animal state	Resting State Recordings	EEG % Suppression	% Isoflurane	Heart rate (BPM)
Light	9	0.37 ± 0.51	1.13 ± 0.21	227.11 ± 43.68
Semi-deep	4	35.78 ± 28.87	1.91 ± 0.12	221.3 ± 33.07
Deep	3	98.73 ± 2.12	2.08 ± 0.14	220.8 ± 44.18

All values are mean ± SD. EEG was recorded continuously, whereas values for isoflurane and heart rate (HR) were discrete and logged at regular intervals.